



Activation or passivation: Influence of halogen dopant (F, Cl, Br) on photothermal activity of Mn₂O₃ in degrading toluene

Xiao Yu, Mengyi Shi, Yixuan Fan, Lixia Yang*, Jie Zhang, Wei Liu, Weili Dai, Shuqu Zhang, Lei Zhou, Xubiao Luo, Shenglian Luo

Key Laboratory of Jiangxi Province for Persistent Pollutants Control and Resources Recycle, Nanchang Hangkong University, Nanchang 330063, Jiangxi Province, China



ARTICLE INFO

Keywords:
Mn₂O₃
Halogen doping
Toluene
Photothermal catalysis
Oxygen vacancy

ABSTRACT

Mn₂O₃ is an exceptional earth-abundant mineral that has been extensively applied in catalytic oxidation because of the strong redox couples like Mn³⁺/Mn²⁺ and Mn⁴⁺/Mn³⁺ exposed on Mn₂O₃ surface. Herein, the catalytic activity of Mn₂O₃ in photothermal degradation of toluene was regulated by halogens including F⁻, Cl⁻ and Br⁻. As the electronegativity ordered in F (3.98) > O (3.44) > Cl (3.16) > Br (2.96), F⁻ doped Mn₂O₃ overperforms Cl⁻ doped and Br⁻ doped Mn₂O₃ in decomposing toluene. DFT theoretical calculation illustrates that F⁻ attracts the shared electrons from Mn to itself, the deviated charge center stretches the adjacent Mn-O bonds and boosts the generation of abundant oxygen vacancies, helping to strengthen the catalytic activity of Mn₂O₃. Conversely, Mn-O bonds are shortened by Cl⁻ and Br⁻ that have lower electronegativity than O. The multiple electrons circling Cl⁻ and Br⁻ push Mn towards O and squeeze Mn-O bonds, resulting in the formation of passivated Mn₂O₃. In conjunction with Mn redox couples and oxygen vacancies, 99% of 400 ppm toluene can be eliminated by F⁻ doped Mn₂O₃, corresponding mineralization rate is high up to 95.8%.

1. Introduction

Volatile organic compounds (VOCs), are mainly human-made chemicals that have a high vapor pressure and low water solubility. The origin of VOCs contains indoor sources and outdoor sources. For instance, building materials (paint, adhesives, pressed wood products), home and personal care products (pesticides, fuel oil, gasoline), as well as activities like smoking, wood burning in stoves, dry-cleaned clothing contribute to indoor air pollution. Industrial emissions, diesel emissions, and oil and gas extraction and processing account for outdoor air pollution. Breathing VOCs probably present a health risk, especially those long-term exposures to benzene, toluene, and formaldehyde that give rise to cancer [1,2]. Toluene, one of the representative aromatic hydrocarbons, has numerous commercial and industrial applications: it is a common solvent in paints, lacquers, thinners, glues, correction fluid, and nail polish remover, as well as in printing and leather tanning procedures [3]. Its wide variety of purposes makes it ubiquitous in atmospheric circumstances. However, inhaling, direct contact, and ingestion bring harmful influences for human beings. Thereby, scientists have placed a premium on cleaning toluene from the air by exploring various techniques that can be classified into two categories: physical

methods and chemical methods. Adsorption with active carbon [4], and membrane separation [5] are included in a physical group, for they only transfer toluene from one place to another without changing their molecular structures. Thermal catalysis [6,7], plasmonic catalysis [8,9], photocatalysis [10,11], photo-thermal catalysis [12,13], and biodegradation technologies [14,15] that can render decomposition of toluene are defined as chemical techniques. Among them, photo-thermal catalysis is an emerging technology using sunlight as an energy source to increase catalyst temperature and trigger chemical reactions, which realizes energy-saving and high efficiency through merging the advances of photocatalysis and thermal catalysis. During photothermal catalysis, upon harvesting solar lights, semiconductor catalysts are capable of converting light energy into heat by demonstrating a broad absorption of the solar spectrum. Simultaneously, they are excited to generate excitons that will be responsible for photocatalysis. As a consequence of conjugating countless active and heated sites, converting toluene is speeded up and toluene molecules can be turned in non-toxic CO₂ and H₂O under mild conditions [16].

Plasmonic catalysts like noble metal nanoparticles engineered semiconductors generally deliver attractive photothermal catalytic activity because of the localized surface plasmon resonance (LSPR) effect

* Corresponding author.

E-mail address: yangliax829@163.com (L. Yang).

[17]. Compared with plasmonic noble metal NPs mediated catalysts, activated carbon (AC)/graphitic carbon nitride (CN) composites [18], CeMn_xO_y/TiO₂ [19], Co₃O₄/TiO₂ [20], CeO₂/LaMnO₃ [21] composites are also able to transfer photos into heat by demonstrating an outstanding photo-thermal catalytic performance, which can compete with plasmonic catalysts.

Manganese oxide (MnO_x) is another promising candidate for photo-thermal catalytic degradation of VOCs due to its excellent activity, good stability, and low cost [22]. The electrons transfer between Mn²⁺, Mn³⁺, and Mn⁴⁺ greatly contributes to the superior catalytic performance of MnO_x during thermal catalysis [23]. For instance, manganese oxide octahedral molecular sieves (OMS-2) exhibited excellent catalytic performance for benzene oxidation by a great deal of oxygen vacancy and its ability in converting solar energy to thermal energy [24]. Mn₂O₃ composites including LaMnO₃ [21], La_{1-x}Ce_xMnO₃ [25], FeMnO₃ [26], NiMnO₃ [27] and SmMnO₃/CuMnO_x [28] demonstrate remarkable photothermal efficacy in removing organic chemicals. Besides the redox couples of Mn, it is found that oxygen vacancy (Ov) in MnO_x accounts for the final degradation efficiency [29,30]. OVs are the most active sites in photocatalysis, which boosts the generation of superoxide radical (•O₂⁻) that account for the strengthened adsorption and degradation of target pollutants. Generally, OVs are created by replacing lattice oxygen with foreign species such as doping or constructing heterojunctions [31]. In Yang's work [32], they controlled the mole ratio of O to Cl through tuning the glucose amount, generating Cu₂O-CuCl composites with plentiful OVs. BiOX (where X = F, Cl, Br, I) are regulated with abundant oxygen vacancy defects owing to X dopant, having superior capacity in adsorbing and activating CO₂ molecules [33]. Fluorine was first used to improve the activity of TiO₂ by adding a small amount of trifluoroacetic acid (TFA) into the sol-gel (SG) starting solution [34]. It was found that fluorine would influence the photocatalytic reactions by changing the interfacial e⁻/h⁺ transfer, surface charge distribution, and substrate-surface interaction, which were attributed to the enhancement of surface acidity, formation of surface hydroxyl radicals, and creation of oxygen vacancies [35]. The F atom tends to substitute lattice O atom in metal oxide because of the similar size compatibility [36]. The aforementioned studies suggest that doping halogens in photocatalysts are efficient and feasible in creating OVs.

Though halogens are common in many precursors for synthesizing MnO_x catalysts and are probably residual in MnO_x, there is no related work about elucidating the influence of fluorine, chlorine, bromine ions on MnO_x's activity and the involved mechanism from the perspective of halogen's electronegativity. Inspired by that, F⁻, Cl⁻, and Br⁻ were doped in Mn₂O₃ and corresponding performance was assessed by applying halogen-Mn₂O₃ in toluene degradation under simulated full-spectrum solar lights. It's found that many more oxygen vacancies are created as Mn₂O₃ is doped with F⁻ on the strength of the marvelous property of attracting shared electrons, which helps to boost the removal efficiency of toluene. As for Cl⁻ and Br⁻, the opposite impact is observable. For the sake of large size and lowered electronegativity compared with O, their doping causes shortened and reinforced Mn-O bonds, which passivates Mn₂O₃ and blocks the active sites, resulting in declined degradation efficacy. This study highlights the influence of fluorine, chlorine, bromine ions upon the photo-thermal activity of Mn₂O₃ catalysts, figuring out the root cause for the variability using different manganese salts with halogen ions contained.

2. Experimental

2.1. Chemicals

Manganese fluoride (MnF₂) was purchased from Shanghai Yuanye Bio-Technology Co., Ltd. Manganese chloride hexahydrate (MnCl₂·4H₂O, 99.99%), Manganese acetate tetrahydrate (C₄H₆MnO₄·4H₂O), and ethanedioic acid dihydrate (C₂H₂O₄·4H₂O) were purchased from Sinopharm Chemical Reagent Co., Ltd. Manganese

bromide tetrahydrate (MnBr₂·4H₂O, 99.99%) was purchased from Aladdin Reagents (Shanghai) Co., Ltd. All these chemicals were of analytical grade and used without further purification.

2.2. Synthesis of catalysts

Mn₂O₃ and Mn₂O₃ doped with fluorine, chlorine, bromine was synthesized by the co-precipitation method. 50 mmol C₄H₆MnO₄ was dissolved in a beaker with 100 mL of deionized water and the solution was kept stirring for 15 min; 60 mmol C₂H₂O₄·4H₂O that was ensured Mn²⁺ was completely precipitated was dissolved in 100 mL of deionized water. The prepared C₂H₂O₄ solution was dropped wisely added to the C₄H₆MnO₄ solution, which was then stirred for 30 min to form a milky MnC₂O₄ suspension. The as-prepared MnC₂O₄ was dried at 60 °C for 8 h and then calcined at 500 °C in static air for 2 h (heating rate 5 °C/min) to obtain Mn₂O₃ (denoted as Mn₂O₃).

Mn₂O₃-F (0.1 mol), Mn₂O₃-Cl (0.1 mol), and Mn₂O₃-Br (0.1 mol) were synthesized in the same way as above with changing partial manganese precursor as MnF₂, MnCl₂·4H₂O and MnBr₂·4H₂O. Taking F⁻ doped Mn₂O₃ as an example kept the total molar amount of Mn (50 mmol) unchanged and regulated the molar ratio of MnF₂ to C₄H₆MnO₄ as 6:4, 4:6, 3:7, 2:8, respectively. The corresponding engineered Mn₂O₃ with different fluorine content was labeled as Mn₂O₃-F (0.06 mol), Mn₂O₃-F (0.04 mol), Mn₂O₃-F (0.03 mol), and Mn₂O₃-F (0.02 mol).

2.3. Characterization

XRD patterns of Mn₂O₃ and halogen doped Mn₂O₃ were obtained with a Bruker D8 Advance X-ray diffractometer (Bruker, Germany) using Cu K α radiation ($\lambda = 1.542 \text{ \AA}$). Atomic ratios of elements in Mn₂O₃ catalysts were analyzed by an energy-dispersive portable X-ray Fluorescence Spectrometer (XRF) using a PANalytical Axios configured in a laboratory accessory stand. X-ray photoelectron spectroscopy (XPS) analyses were carried out in an ultrahigh vacuum chamber with a pressure of 2×10^{-9} bar at room temperature (Thermo Fisher Scientific, ESCALAB 250). The morphology and microstructures of catalyst were observed with the transmission electron microscope (TEM) (FEI Talos F200X) and scanning electron microscopy (SEM) (Hitachi, model SU1510). UV-Vis-IR spectrophotometer (UV-3600 plus) was employed to record the full-spectrum light absorption on Mn₂O₃ catalysts. EPR and ESR spectra were obtained through an electron paramagnetic resonance spectrometer (Bruker A300). Laser Raman spectrum was measured with Ar ion laser as the excitation source, and the test range was about 50–800 cm⁻¹ frequency band (HORIBA Jobin Yvon S. A. S.). H₂ temperature-programmed reduction (H₂-TPR) and O₂ temperature-programmed desorption (O₂-TPD) were carried out on the AutoChem1 II 2920 chemical adsorption analyzer. The temperature images were measured using a FLIR infrared thermometer. The relative humidity was measured using a humidity/temperature transmitter (HMT130). The BET adsorption and desorption isotherms were performed on a Belsorp-Mini II analyzer (Japan), which relative uncertainty is $\pm 7\%$. A thermocatalytic reaction was carried out in a thermostatic heating jacket (ZNCL-T). Gas chromatography (GC, Agilent Technologies 7890A) was used to detect the concentration of toluene and CO₂ in the catalytic process, and gas chromatography-mass spectrometry (GC-MS, Agilent Technologies 7890A-5975C) was used to identify the specific components in the reactor during the catalytic process.

2.4. Photo-thermal degradation of toluene with Mn₂O₃ and halogen-Mn₂O₃

The solar light-driven thermocatalytic oxidation of toluene was performed in a closed cylindrical stainless steel gas-phase reactor (450 mL) equipped with a quartz window (110 mm in diameter). In the reactor, the air was regulated according to the components in actual air. The content of N₂ is 78%, that of O₂ is 21%, and the relative humidity

ranges from 5% to 100%. The reactor was connected to a GC-MS gas chromatograph (GC) equipped with a flame ionization detector (FID) for in-situ monitoring intermediates generated during toluene degradation. 0.1000 g catalyst was uniformly coated on a glass fiber filter membrane (50 mm in diameter and 0.1 μm aperture), which was subsequently placed on the reactor bottom. A 300 W Xe lamp (Perfect Light, PLS-SXE300) was placed above the quartz window to provide UV-Vis-NIR lights (Light intensity: 398 mW/cm²). The temperature change during the reaction was determined by a FLIR infrared thermometer.

CO₂ increase was taken as an indicator to evaluate the mineralization degree of toluene. As there are CO₂ molecules in the air and the catalysts can adsorb CO₂, the reactor needed to be irradiated for 15 min to reach a steady CO₂ baseline for the subsequent determination of CO₂ increment, and then turned off the light. Soon after that, 0.86 μL of liquid toluene was injected into the reactor through an inlet embedded in the hermetic seal. The calculated initial toluene concentration is about 400 ppm. 5 min later, after all the toluene molecules evaporated, turned on the lamp, and started the degradation. CO₂ increment was recorded by subtracting the initial CO₂ content (before catalysis) in the reactor, and the corresponding removal percentage of toluene was calculated. Repeated runs were conducted under the same conditions after renewing the reactor with fresh air.

2.5. DFT theoretical calculation

We employed a Vienna Ab Initio Package (VASP) [37,38] to perform all the density functional theory (DFT) calculations within the generalized gradient approximation (GGA) using the PBE formulation [39]. The projected augmented wave (PAW) [40,41] potentials were employed to describe the ionic cores and take valence electrons into account using a plane-wave basis set with a kinetic energy cutoff of 450 eV. Partial occupancies of the Kohn-Sham orbitals were allowed using the Gaussian smearing method and a width of 0.05 eV. The electronic energy was considered self-consistent when the energy change was lower than 10⁻⁴ eV. Geometry optimization was considered convergent when the force change was less than 0.05 eV/Å. Grimme's DFT-D3 methodology was used to describe the dispersion interactions [42]. The equilibrium lattice constants of the Mn₂O₃ unit cell were optimized when using a 5 \times 5 \times 5 Monkhorst-Pack k-point grid for Brillouin zone sampling. The vacuum spacing perpendicular to the plane of the structure was 20 Å. The Brillouin zone integral uses the surfaces structures of 3 \times 3 \times 1 monkhorst pack K point sampling for surfaces. The formation energies of O was calculated as follow:

$$E_f = E_{\text{total}} - \frac{1}{2}E_{\text{O}_2} + xE_B$$

where the E_{total} is Mn₂O₃ with M (F, Cl, Br) doping energy with O defect and E_B is the structure energy, E_{O2} is the O₂ energies. The adsorption energies (E_{ads}) were calculated as:

$$E_{\text{ads}} = E_{\text{ad/sub}} - E_{\text{ad}} - E_{\text{sub}}$$

where E_{ad/sub}, E_{ad}, and E_{sub} are related to the optimized adsorbate/substrate system, the adsorbate on the catalyst surface, and the clean substrate, respectively.

3. Results and discussion

3.1. Morphological and structural characterization of Mn₂O₃ and Mn₂O₃-halogen

XRD patterns (Fig. 1) show that Mn₂O₃ catalysts doped with F⁻, Cl⁻ display almost the same diffraction peaks as those of pristine Mn₂O₃. The specific peaks located at 66.2°, 55.3°, 49.5°, 45.5°, 38.8°, 33.1°, and 23.3° correspond to the crystal planes of (622), (440), (431), (332), (400), (222), and (211), respectively, which are indexed to cubic bixbyite Mn₂O₃ [43]. Nevertheless, compared with pristine Mn₂O₃, the enlarged diffraction peaks at 33.1° exhibit that the (222) plane of Mn₂O₃-F positively shifts, indicating a shrank lattice spacing. As for Mn₂O₃-Cl and Mn₂O₃-Br catalysts, slightly negative shifts are observable, suggesting the lattice spacings along (222) planes are widened.

Based on the XRD data in Fig. 1, the lattice constant values (a) of pristine and halogen-doped Mn₂O₃ were calculated using the following equation [44]:

$$d^2 = \frac{a^2}{h^2 + l^2 + k^2}$$

Where d is the interplanar distance, a is the lattice parameter, and h, k, l are the miller indices of the crystal plane. Since α -Mn₂O₃ is a cubic phase, the lengths a, b, and c of the three cell edges are equal. As shown in Table S1, the edge length of Mn₂O₃ unit cell is decreased from 9.4091 Å to 9.3955 Å in Mn₂O₃-F while those in Mn₂O₃-Cl and Mn₂O₃-Br are prolonged to 9.4222 Å and 9.4227 Å, respectively. Fig. 1 and Table S1 verify the lattice contraction aroused by F⁻ and lattice expansion triggered by Cl⁻ and Br⁻.

The effect of increased calcination temperatures was studied. As Fig. S1 depicted, a higher temperature treatment enables a higher crystallinity of Mn₂O₃ with strong Mn-O covalent bonds, which will

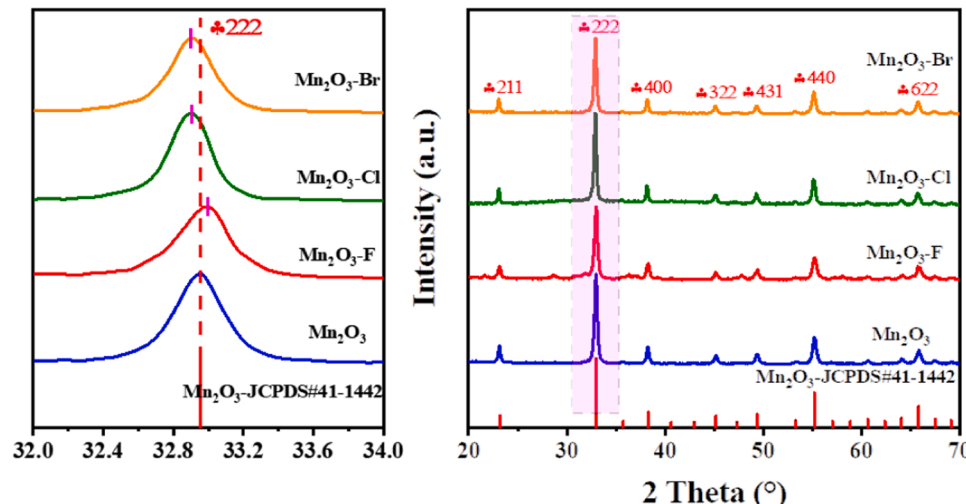


Fig. 1. XRD patterns of pristine Mn₂O₃ and Mn₂O₃ doped with F⁻, Cl⁻, Br⁻.

make it difficult for halogens to bond with Mn. Our investigation validates that 500 °C is the optimal calcination temperature for synthesizing pure Mn₂O₃ with suitable crystallinity. Depicted as Fig. S1a, the products are predominantly Mn₃O₄ when the MnC₂O₄ (0.1 mol F) precursor was subjected to calcination at 400 °C. As the temperature increased to 600 °C, the crystallinity of Mn₂O₃ is notably enhanced. Consequently, the content of OVs in Mn₂O₃ is less than that sintered at 500 °C (Fig. S1b). Moreover, the bond predominates in the halogen-Mn₂O₃ compound is still a covalent bond, for the Mn-Cl bonds are in small quantities.

Although SEM images of Mn₂O₃ and halogen-Mn₂O₃ (Fig. 2) exhibit that the as-prepared are big blocks covered with cracks, the nitrogen adsorption-desorption isotherms (Fig. S2) of the different Mn₂O₃ catalysts show type-IV curves with H3 hysteresis loop at relatively high pressure ($0.6 \leq P/P_0 \leq 1.0$), demonstrating the mesoporous features [21]. Listed as Table S1, the Brunauer-Emmett-Teller (BET) surface area of Mn₂O₃ is 16.9 m²/g, doping F⁻ (0.03 mmol in precursor) in Mn₂O₃ improves BET to 32.4 m²/g. The total pore volume is increased from 0.18 to 0.27 cm³/g, and the average pore diameter is shrunk from 41.5 to 33.5 nm. However, doping Cl⁻ and Br⁻ in Mn₂O₃ brings a negative impact on Mn₂O₃ construction. The specific surface area of Mn₂O₃-Cl and Mn₂O₃-Br are less than 10 m²/g. As Cl⁻ and Br⁻ have larger ion radii than F⁻, their doping contents in Mn₂O₃ are minor than that of F⁻ in Mn₂O₃. Except those implanted in Mn₂O₃, some residual Cl⁻ and Br⁻ are adsorbed on the Mn₂O₃ surface, covering the active centers [45]. Moreover, during the synthesis process of Mn₂O₃-Cl and Mn₂O₃-Br, the dispersed Cl⁻ and Br⁻ also suppress the cleavage of crystals and the generation of small particles during calcination [46], leading to the decline in specific surface areas.

TEM images in Fig. 2 present the details of structural varies caused by

halogen doping. As shown, all the Mn₂O₃ catalysts are in nanoparticle form, which tends to aggregate to form a mesoporous interface. Although the nanoparticles are in irregular shapes, their diameters are less than 10 nm. Comparing the high-resolution TEM images, the lattice spacing indexed to (222) planes in Mn₂O₃-F is 0.263 nm, less than the 0.272 nm in pristine Mn₂O₃, while those among Mn₂O₃-Cl, Mn₂O₃-Br lattice fringes are 0.274, 0.276 nm, respectively, increased by 0.002 and 0.004 nm as compared with the standard 0.272 nm.

The variation in Mn₂O₃ structure posed by F⁻ doping is more significant than Cl⁻ and Br⁻ doping, and the changing trends in lattice spacing are in accordance with the XRD analysis. Moreover, as the elemental mapping pictures (Fig. 2) of F⁻, Cl⁻, and Br⁻ show, the loading content of F⁻ in Mn₂O₃ is much higher than those of Cl⁻ and Br⁻. That's because F⁻ is the smallest, its diameter is 0.133 nm, almost as same as that of O²⁻ (0.14 nm), which enables F⁻ to enter Mn₂O₃ lattice and replace O more easily. It was also reported that the heteroatom tends to substitute an atom with the same approximate valence state and size compatibility [47]. Concerning Cl⁻ (0.181 nm) and Br⁻ (0.196 nm), their large sizes hinder the insertion in Mn₂O₃, leading to low doping contents. Since XRF is a rigorous method for ascertaining the contents of elements in the matrix, it was employed to determine the atomic ratio of F, Cl, and Br in Mn₂O₃ catalysts. As shown in Table S2, the atomic ratios of F, Cl, Br in Mn₂O₃-F, Mn₂O₃-Cl, Mn₂O₃-Br determined by XRF are 6.42%, 4.28%, and 1.98% accordingly, minimized with the increased ion radius of F, Cl, and Br. XPS and TEM analysis on element contents were conducted as well. Relating results in Table S2 show that although the specific values from different strategies are variable, they demonstrate the same tendency, which confirms that F⁻ can be implanted in Mn₂O₃ with higher contents due to its smallest size.

Nevertheless, depicted in Fig. S3, overloading of F⁻ in Mn₂O₃ causes

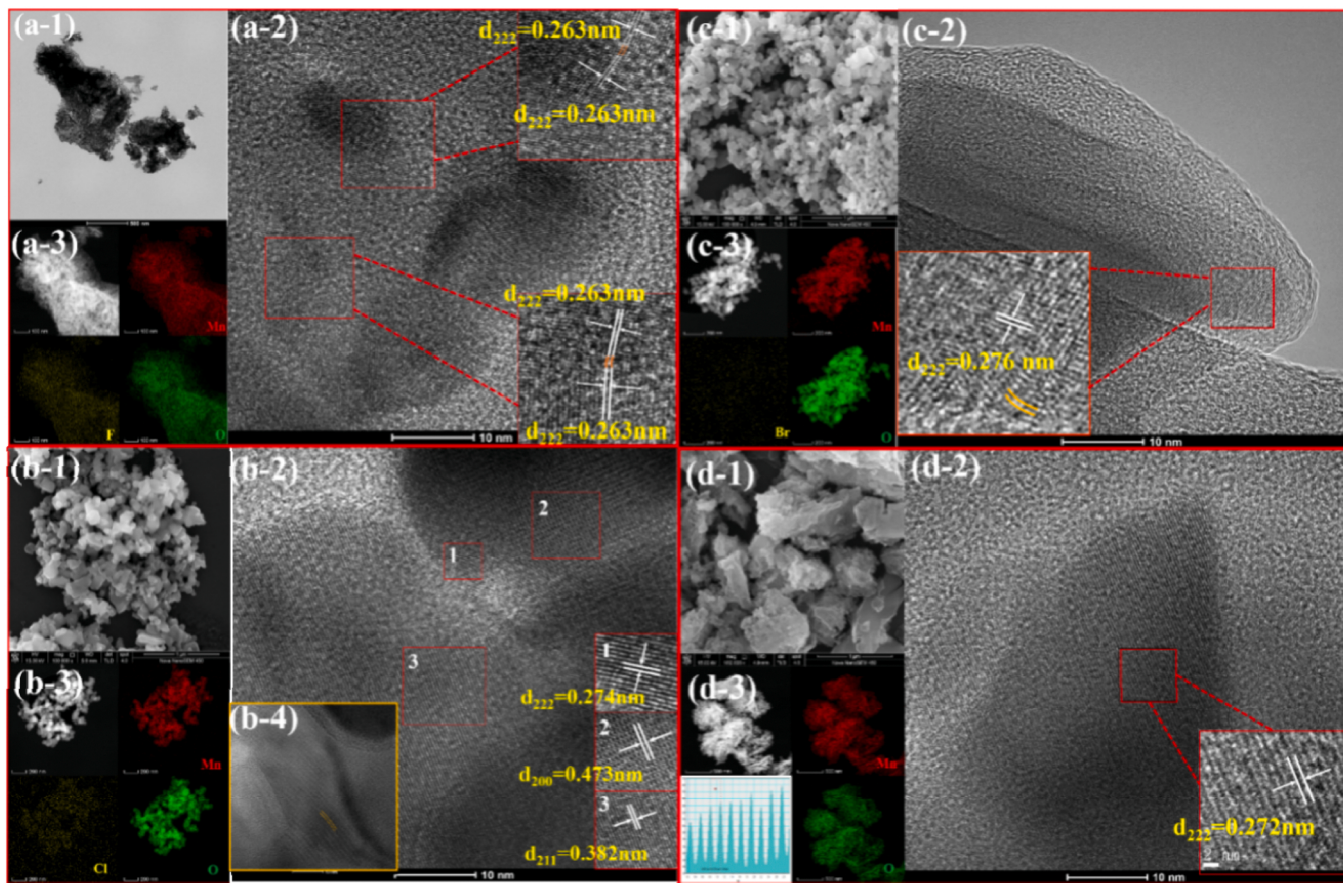


Fig. 2. SEM, HRTEM, and EDS phase mapping of the Mn (red), halogen (yellow), and O (green) distributions images of the (a) Mn₂O₃-F, (b) Mn₂O₃-Cl, (c) Mn₂O₃-Br, and (d) Mn₂O₃ catalysts.

declined crystallinity along (222) planes. Increasing Cl^- and Br^- dopant pose the same results as that of F^- .

3.2. Textural property of as-prepared Mn_2O_3 and halogen- Mn_2O_3

XPS spectra of Mn 2p in Fig. 3a show characteristic peaks centered at 641.79 eV and 653.51 eV, which are assigned to Mn 2p 3/2 and Mn 2p 1/2, respectively. Each peak can be deconvoluted into three peaks according to the binding energies of Mn species, Mn^{2+} , Mn^{3+} , and Mn^{4+} [48]. Compared with pristine Mn_2O_3 , the binding energies of Mn 2p in $\text{Mn}_2\text{O}_3\text{-F}$ positively shift by 0.89 eV, for the sake of decreased electron density around Mn. The root cause behind this is the high electronegativity of F. It's known that electronegativity, symbolized as X, is the tendency for an atom to attract shared electrons (or electron density) when forming a chemical bond. The electronegativity of F is the strongest among all the elements. $X(\text{F})$ is 3.98, higher than $X(\text{O})$ 3.44. When O^{2-} in Mn_2O_3 is replaced by F, the electrons circling Mn are attracted by F and incline to F, leading to the increased binding energy of valence electrons in Mn 2p orbits. The opposites occur in presence of Cl^- and Br^- doping because $X(\text{Cl})$ is 3.16, $X(\text{Br})$ is 2.96, both less than $X(\text{O})$.

Furthermore, the redox couples, $\text{Mn}^{2+}/\text{Mn}^{3+}$ and $\text{Mn}^{3+}/\text{Mn}^{4+}$, in Mn_2O_3 help to transfer photogenerated electrons among $\text{Mn}^{2+}\text{-Mn}^{3+}\text{-Mn}^{4+}$ circle for benefiting the photocatalysis [49]. The proportions of Mn^{x+} ($x = 2, 3, 4$) on the MnO_x surface determine the surface oxygen species [50]. In general, numbers of surface adsorbed oxygen species like O^{2-} or O^- rely on Mn^{4+} content. And Mn^{2+} accounts for the production of oxygen vacancy. Therefore, high contents of Mn^{4+} and Mn^{2+} will strengthen the oxidizing capacity of MnO_x . According to the Mn 2p XPS spectra (Fig. 3a), the proportions of Mn^{2+} , Mn^{3+} , Mn^{4+} were calculated through quantitative analysis, corresponding data are listed in Table S3. Among all the halogen-doped Mn_2O_3 catalysts, F dopant boosts the most notable enhancement in the contents of Mn^{2+} and Mn^{4+} , accompanied by the lowest Mn^{3+} contents. The proportions of Mn^{2+} , Mn^{3+} , Mn^{4+} in the pristine Mn_2O_3 are 2.44%, 54.72%, and 42.83% in sequence, which vary as 5.21%, 43.25%, and 51.64% in $\text{Mn}_2\text{O}_3\text{-F}$, verifying the active role of F dopant.

Fig. 3b shows the UV-Vis-NIR absorption spectra of different Mn_2O_3 catalysts which are all sensitive to full-spectrum light. The strong absorption bands in wavelength ranges of 250–300, 650–750, 1350–1450, and 2100–2400 nm are observable, and $\text{Mn}_2\text{O}_3\text{-F}$ demonstrates the optimal capacity of light harvest. Temperature images are captured using a FLIR infrared thermometer. As the inset in Fig. 3b displays, under irradiation, the temperatures of Mn_2O_3 , $\text{Mn}_2\text{O}_3\text{-F}$, $\text{Mn}_2\text{O}_3\text{-Cl}$, and $\text{Mn}_2\text{O}_3\text{-Br}$ reach 198 °C, 213 °C, 196 °C, and 199 °C, respectively. Although the four catalysts display similar absorption peaks within the full-spectrum light region, only F doping realizes the enhancement in photothermal conversion, which can be ascribed to the increasing structural defects and the increased Brunauer-Emmett-Teller (BET) surface areas of Mn_2O_3 [51,52].

H_2 temperature-programmed reduction ($\text{H}_2\text{-TPR}$) profiles depicted in Fig. 3c exhibit two reduction peaks, the one located at 332 °C is from Mn^{4+} being reduced to Mn^{3+} , the other at 441 °C stands for the conversion of Mn^{3+} to Mn^{2+} , which illustrates the stepwise reduction of Mn_2O_3 to Mn_3O_4 , and ultimately to MnO [43]. Usually, the temperature for Mn_2O_3 transforming in Mn_3O_4 is used to evaluate the reduction capacity of Mn_2O_3 . Compared to the pristine Mn_2O_3 , doping F Mn O_3 can enable Mn ions reduced at lower temperatures, implying that $\text{Mn}_2\text{O}_3\text{-F}$ can accept electrons more easily than Mn_2O_3 . On the contrary, the elevated temperatures presented by $\text{Mn}_2\text{O}_3\text{-Cl}$ and $\text{Mn}_2\text{O}_3\text{-Br}$ suggest that Mn_2O_3 is passivated by Cl^- and Br^- . And concerning the effect of doping amount of F amount, the most significant decrease of temperature is achieved on $\text{Mn}_2\text{O}_3\text{-F}$ (0.03 mol). O_2 temperature-programmed desorption ($\text{O}_2\text{-TPD}$) analysis was performed to identify the types of oxygen species in Mn_2O_3 for exploring the potential factors affecting the reduction properties [48]. Generally, the oxygen species (peroxide species, O_2^-) can be classified as the surface oxygen species (<350 °C),

active lattice oxygen species (monatomic species, O^-) near the surface (350–550 °C), and lattice oxygen species (also known as O^{2-} species, >550 °C) [43]. Much attention has focused on the first two because lattice oxygen species (O^{2-} species, >550 °C) often become inert during toluene oxidation at low temperatures [53]. Profiled as Fig. 3d, all $\text{Mn}_2\text{O}_3\text{-F}$ candidates display intense signals (active lattice oxygen species) sited at 526 °C, which manifests the exceptional oxidizing capacity of $\text{Mn}_2\text{O}_3\text{-F}$. As for $\text{Mn}_2\text{O}_3\text{-Cl}$ and $\text{Mn}_2\text{O}_3\text{-Br}$, they exhibit declined performance than the pristine Mn_2O_3 .

A theoretical model was established with density functional theory (DFT) to further illuminate the influence mechanism of halogen doping. In the light of Fig. 3e, the calculated band energy of Mn-O in original Mn_2O_3 is 206.63 kJ/mol, which goes down to 172.96 kJ/mol in $\text{Mn}_2\text{O}_3\text{-F}$ along with the Mn-O bond length extends from 2.37 Å to 2.44 Å. The various evidence that F weakens the adjacent Mn-O bonds by stretching them, signifying Mn_2O_3 is activated. However, because of the lower electronegativity compared with O (3.44) and the big ion radius, doping Mn_2O_3 with Cl (3.16) and Br (2.96) renders shortened Mn-O bands in $\text{Mn}_2\text{O}_3\text{-Cl}$ and $\text{Mn}_2\text{O}_3\text{-Br}$: 2.24 Å for $\text{Mn}_2\text{O}_3\text{-Cl}$, 2.21 Å for $\text{Mn}_2\text{O}_3\text{-Br}$, presented as increased bond energies: 219.24 kJ/mol and 232.14 kJ/mol, respectively. The reinforced Mn-O bonds will be hard to be broken and difficult to supply active lattice oxygen.

3.3. Catalytic performance in the degradation of toluene under different conditions

To address the synergistic catalytic performance, photocatalytic, thermal catalytic, and full-spectrum-light driven photothermal degradation of toluene was carried out to evaluate the impact of F^- , Cl^- , and Br^- on the catalytic activity of Mn_2O_3 , with results shown in Fig. 4a and b. It is found that photocatalysis and thermal catalysis are not as effective as photothermal catalysis. The photothermal removal percentage of toluene on variable Mn_2O_3 catalysts is ordered as $\text{Mn}_2\text{O}_3\text{-F}$ (0.1 mol) (99%) > Mn_2O_3 (85%) > $\text{Mn}_2\text{O}_3\text{-Cl}$ (0.1 mol) (55%) > $\text{Mn}_2\text{O}_3\text{-Br}$ (0.1 mol) (52%). Of note, mineralization endowed by $\text{Mn}_2\text{O}_3\text{-F}$ is high up to 89%, much superior to Mn_2O_3 (72%), $\text{Mn}_2\text{O}_3\text{-Cl}$ (26%), and $\text{Mn}_2\text{O}_3\text{-Br}$ (24%). F doping remarkably improves the final catalytic efficiency in detoxifying toluene by converting it to CO_2 and H_2O , while Cl^- and Br^- bring negative influence. Combining the results in Fig. 3, we conclude that the activated Mn-O bonds in $\text{Mn}_2\text{O}_3\text{-F}$ play a pivotal role in accelerating the decomposition of toluene.

Fig. 4c and d exhibit that the removal percentage of toluene is improved as the F content in Mn_2O_3 increased, after reaching the vertex in presence of $\text{Mn}_2\text{O}_3\text{-F}$ prepared with 0.03 mol of F in precursor, it declines in that over-doping F in Mn_2O_3 could cover and block the active sites implanted in Mn_2O_3 [54]. With the best $\text{Mn}_2\text{O}_3\text{-F}$ (0.03 mol in precursor), the toluene degradation efficiency is 99%, and the mineralization degree is high up to 95.8%. In the following section, all the $\text{Mn}_2\text{O}_3\text{-F}$ mentioned is the optimal one.

We tested the catalytic activity of the $\text{Mn}_2\text{O}_3\text{-F}$ in degrading toluene under irradiation of ultraviolet-visible-infrared, visible-infrared and infrared lights by using different cutoff filters, with results in Fig. 5a and b. The difference in the degradation percentage of toluene under different lights is not notable, but the variability regarding mineralization degree is significant. Driven by UV-Vis-NIR lights, the CO_2 yield is $131.78 \text{ mg m}^{-3} \text{ min}^{-1}$, and that under visible lights (wavelength > 420 nm) is $117.95 \text{ mg m}^{-3} \text{ min}^{-1}$. When only NIR lights above 780 nm are applied, the CO_2 yield is $76.65 \text{ mg m}^{-3} \text{ min}^{-1}$. These results indicate that $\text{Mn}_2\text{O}_3\text{-F}$ is efficient for eliminating toluene even if there is no UV light, exhibiting promising prospects in practical application.

Since H_2O is the source of hydroxyl radicals that is the main oxidants accounting for the photocatalytic degradation of toluene, the influence of relative humidity (RH) on the catalytic performance of $\text{Mn}_2\text{O}_3\text{-F}$ was studied by changing H_2O content in the feed gas. Profiles and histograms in Fig. 5c and d show that the photothermal degradation of toluene and the mineralization efficiency curves rise first and then down with

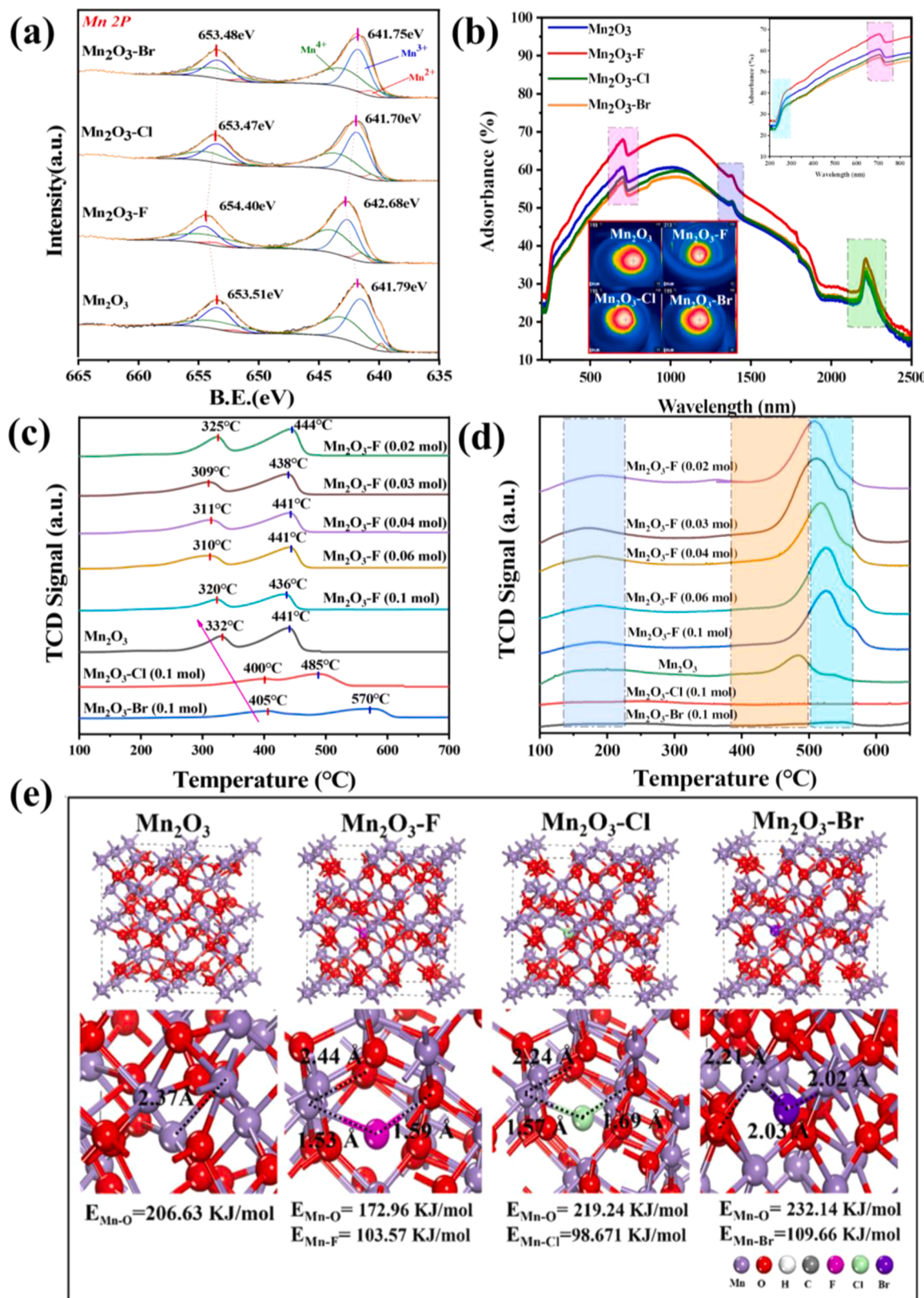


Fig. 3. (a) XPS spectra of Mn 2p, (b)UV-Vis-NIR diffuse reflectance spectra and temperature images of Mn_2O_3 , $\text{Mn}_2\text{O}_3\text{-F}$, $\text{Mn}_2\text{O}_3\text{-Cl}$, and $\text{Mn}_2\text{O}_3\text{-Br}$; (c) $\text{H}_2\text{-TPR}$, (d) $\text{O}_2\text{-TPD}$ analysis about Mn_2O_3 and those doped with halogens, (e) calculated band energies of Mn-O, Mn-F, Mn-Cl, and Mn-Br.

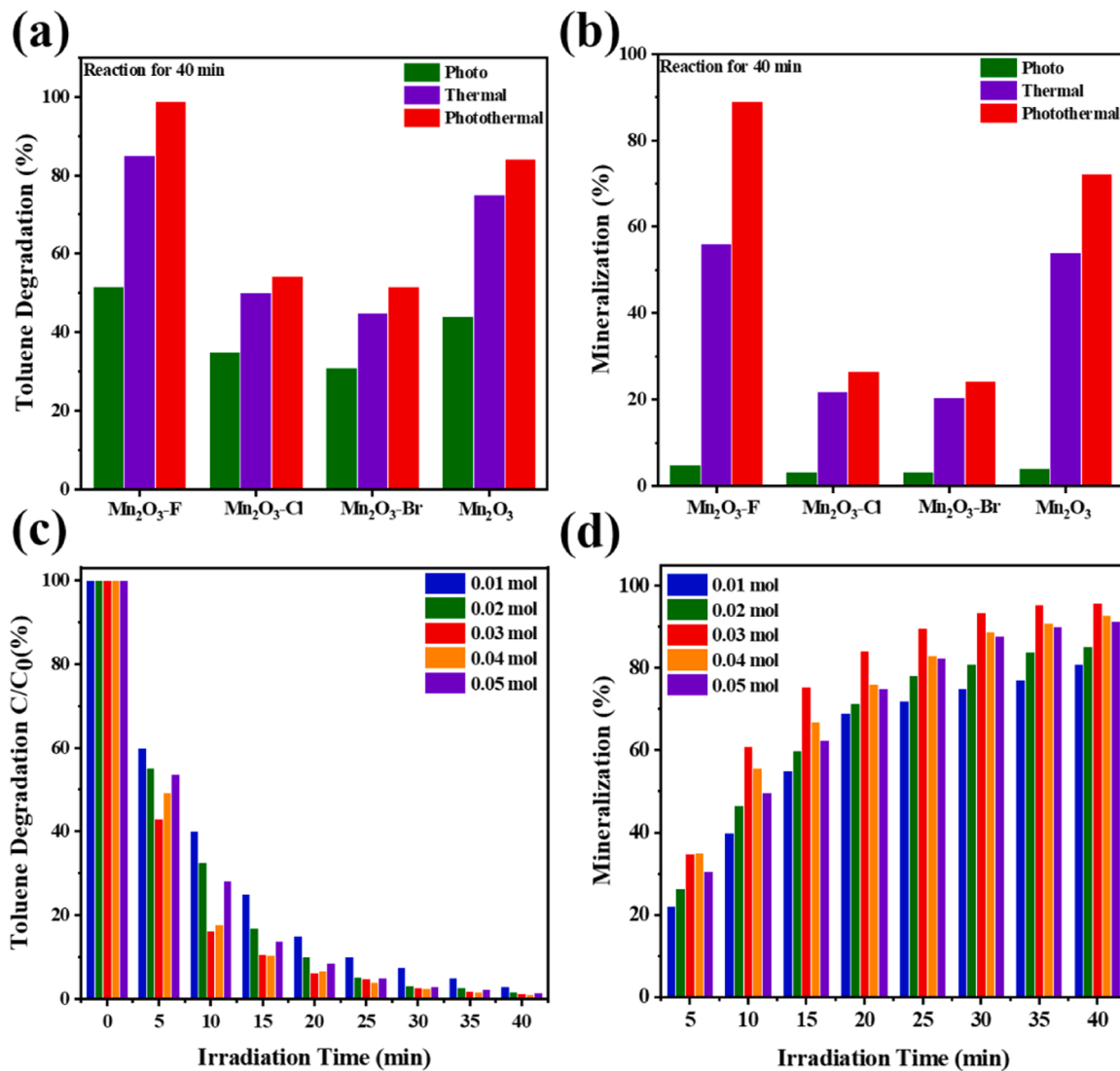


Fig. 4. (a) Degradation percentage of toluene and (b) mineralization degree in 40 min under different conditions including photocatalysis performed at 25 °C (cooled by condensate water), thermal catalysis at 210 °C without lights, and photothermal catalysis under UV–Vis–NIR lights, (c) toluene degradation and (d) mineralization affected by variable F⁻ contents. (Air condition: N₂:78%, O₂:21%, and relative humidity: 50%).

increased RH. The degradation efficiency peaks at RH 60%, 98% removal percentage and 94% CO₂ yield are determined. After that, a higher RH leads to delined catalytic activity, for competitive adsorption occurs between excess H₂O and toluene. Moreover, a thin H₂O membrane may cover the active sites on Mn₂O₃ and then scale back the reaction possibility. As the ambient humidity in the air generally ranges from 40% to 80% [55], the outstanding performance in detoxifying toluene makes Mn₂O₃-F propitious in assembling advanced appliances for high-quality indoor air.

Apart from the high activity, a long lifetime is essential for a promising catalyst. Consecutively repeated degradation of toluene using the same catalyst was performed to assess the stability of optimal Mn₂O₃-F. Corresponding results in Fig. S5 depict that Mn₂O₃-F retains its superior activity even in the 10th test, the mineralization is only decreased by 3.2%, confirming its outstanding durability.

The catalytic performance of Mn₂O₃-F (0.03 mol) in degrading toluene with high concentration and variable typical VOCs were studied as well. As shown in Fig. 6 and Table S4, the optimal Mn₂O₃-F (0.03 mol F) exhibits high efficacy in decomposing toluene when its initial concentration ranges from 400 ppm to 1000 ppm. The removal percentage is 98% at 1000 ppm in 40 min, which can reach 100% with prolonged irradiation time. Different gaseous chemicals like

formaldehyde, n-hexane, xylene, and benzene were selected as targets to evaluate the Mn₂O₃-F's practicability under complex conditions. As depicted, formaldehyde, n-hexane, xylene (Initial concentration: 400 ppm) can be completely converted to CO₂ and H₂O. Regarding benzene, the removal percentage is 88% and the mineralization degree is 79.1%, for the symmetric and stable structure of benzene. Although there is a bit of decline, its performance in detoxifying VOCs is still attractive, evidencing its promising prospect in practice. Additionally, comparing Mn₂O₃-F with those reported in literature like Co₃O₄/TiO₂, W doped MnO₂, CeO₂/LaMnO₃, Mn₂O₃/Mn₃O₄/MnO₂ (Table S5), either the removal percentage or mineralization degree of toluene achieved on Mn₂O₃-F is remarkable.

3.4. Oxygen vacancy produced on Mn₂O₃ catalysts

Based on the above catalytic performance of Mn₂O₃ and halogen-Mn₂O₃ catalysts, it is believed that active oxygen species contribute to the accelerated mineralization of toluene. In Fig. 7a, the O 1s XPS spectrum collected from Mn₂O₃ is deconvoluted into three peaks, containing lattice oxygen at 529.5 eV (O_{lattice}), surface adsorption oxygen species (O_{ad}) at 531.0 eV (induced by O_{vacancy}), and adsorbed hydroxyl groups or water at 533.0 eV (O_{OH}) [56]. Among them, O_{ad} species

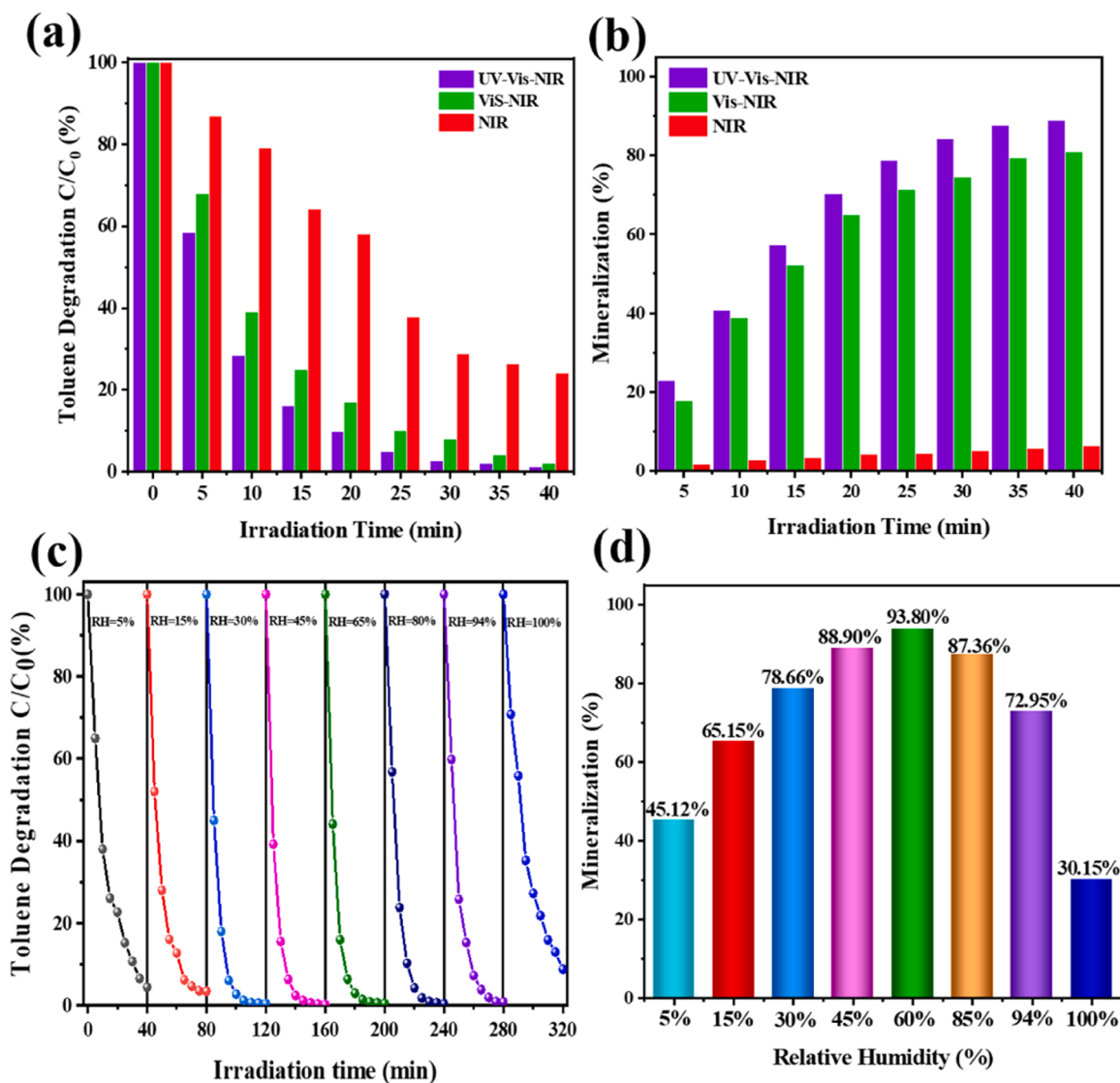


Fig. 5. (a) Toluene removal and (b) mineralization affected by the $\text{Mn}_2\text{O}_3\text{-F}$ under different wavelength lights, (c) degradation of toluene, and (d) mineralization degree affected by variable relative humidity (RH).

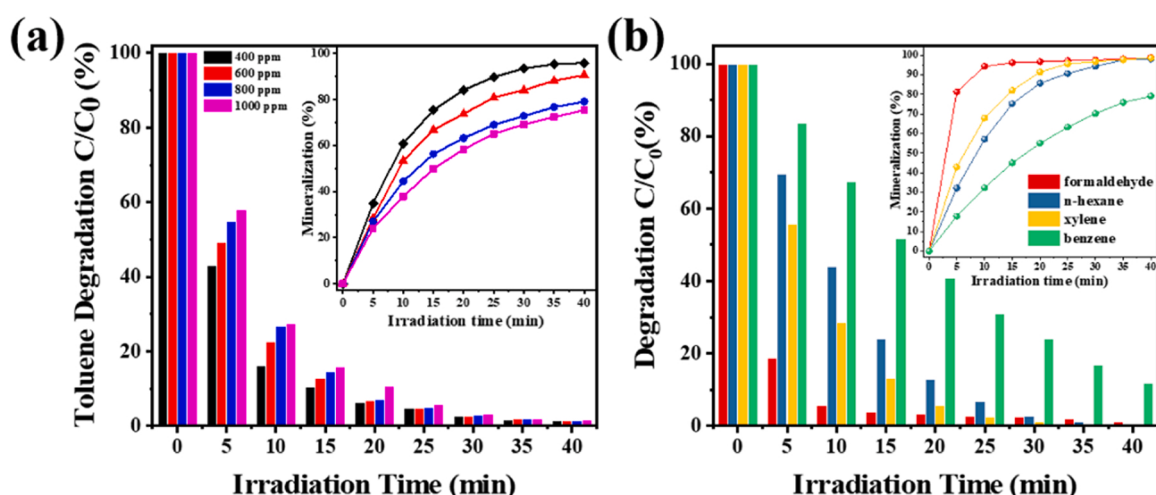


Fig. 6. Toluene removal and mineralization percentage of (a) different concentration toluene and (b) different pollutant species over $\text{Mn}_2\text{O}_3\text{-F}$ (0.03 mol).

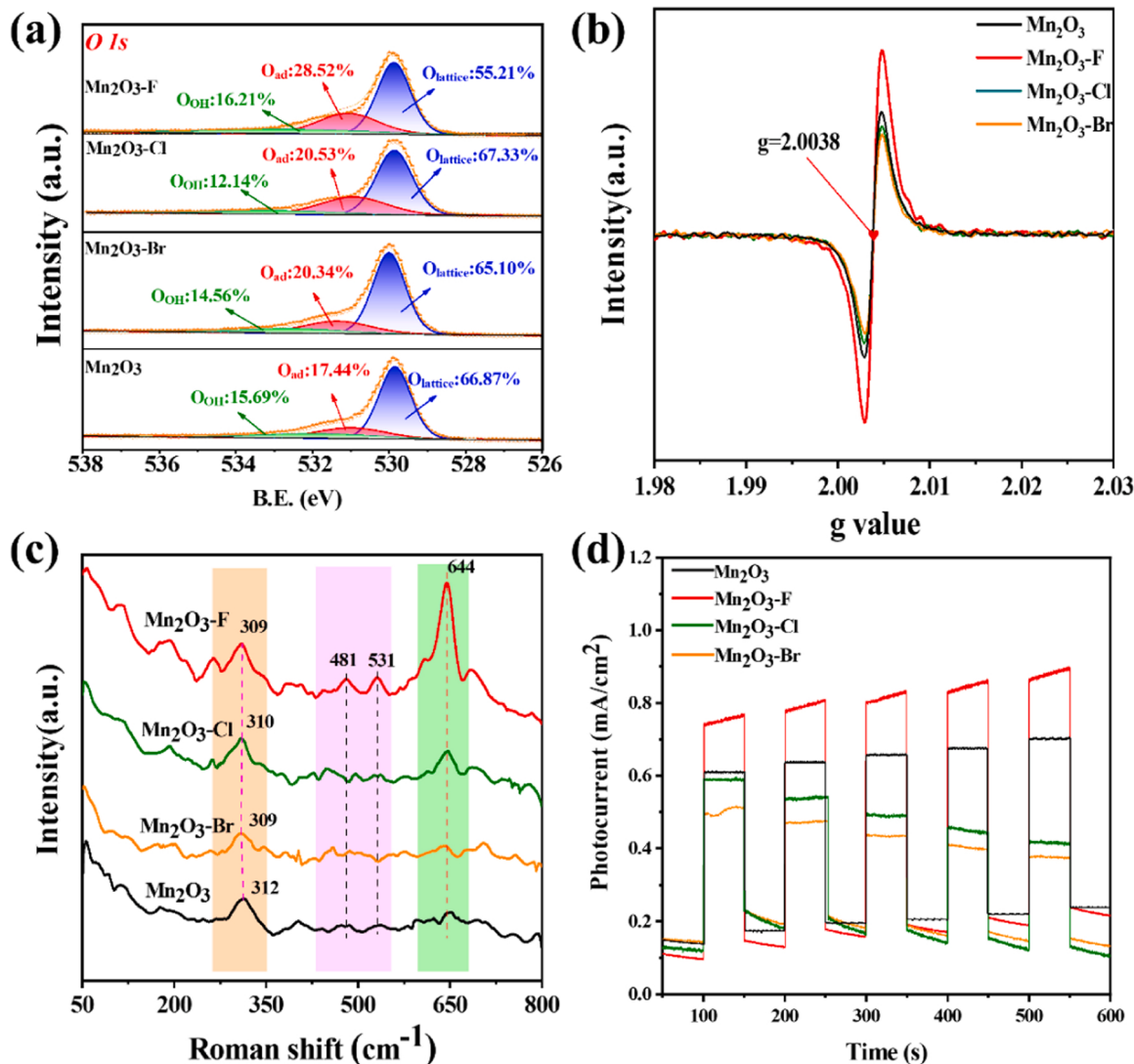


Fig. 7. (a) XPS spectra of O 1s, (b) ESR spectra of oxygen vacancy, (c) Raman spectra, (d) photocurrent intensity.

including O₂[−], O₂^{2−} and O[−] are responsible for the catalytic degradation of target molecules [3,27], which depend on the oxygen vacancies (O_{vs}) implanted in the semiconductor. Namely, more oxygen vacancies, more surface adsorbed active oxygen and higher final degradation efficiency. By integrating the peak area in Fig. 7a, the O_{ad} proportion in Mn₂O₃-F is 28.52%, higher than the 17.44% in Mn₂O₃, 20.53% in Mn₂O₃-Cl, and 20.34% in Mn₂O₃-Br, signifying that there are many more O_{vs} in Mn₂O₃-F. Fig. 7b demonstrates the electron spin resonance (ESR) spectra recorded on Mn₂O₃, and Mn₂O₃ catalysts doped with F[−], Cl[−], and Br[−]. The most intense ESR signal rendered by Mn₂O₃-F demonstrates that Mn₂O₃ is enriched with O_{vs} due to F[−] doping. Instead, bringing Cl[−] and Br[−] in Mn₂O₃ impedes the O_{vs}’s production because of their passivation effect as mentioned above.

To elaborate the creation of O_{vs} in Mn₂O₃, Raman spectra were collected. As Fig. 7c displays, the peaks observed at 309 cm^{−1}, 481 cm^{−1}, 531 cm^{−1}, and 644 cm^{−1} are assigned to the asymmetric stretching mode of the bridging oxygen species (Mn-O-Mn). Notably, Mn₂O₃-F exhibits stronger Raman intensity than all the other Mn₂O₃ catalysts, especially the Raman mode centered at 644 cm^{−1} which is a sign that can prove many more oxygen defects in Mn₂O₃-F [57]. The measurement of transient photocurrent response was carried out to verify the separation of photo-induced carriers in Mn₂O₃ catalysts doped with different halogens (X=F, Cl, Br). As the I-t curves in Fig. 7d depict, Mn₂O₃-F surpasses the pristine ones, Mn₂O₃-Cl, and Mn₂O₃-Br in

generating high-density current.

The relative O_v concentration can be expressed as the average oxidation state (AOS) of Mn 3s in Mn₂O₃ samples, the lower value of AOS, the higher the oxygen vacancy concentration [24], which was calculated based on the multiplet splitting of Mn 3s orbitals according to the following formula:

$$AOS = 8.95 - 1.13\Delta Es(eV)$$

Where ΔEs is the binding energy difference between the main peak and its satellite originated from multiplet splitting in Mn 3s orbitals. The obtained ΔEs of Mn₂O₃, Mn₂O₃-F, Mn₂O₃-Cl, and Mn₂O₃-Br are 5.40, 5.84, 5.59, and 5.47 eV, respectively (Fig. 8). The AOS in Mn₂O₃-F is 2.35 eV, which is the lowest among all the Mn₂O₃ catalysts, revealing its highest O_v content, which is in line with ESR analysis (Fig. 7b).

Furthermore, the O_v formation energies on pristine Mn₂O₃ and halogen-Mn₂O₃ were calculated (Fig. S6). The sequence from high to low is: Mn₂O₃ (1.57 eV) > Mn₂O₃-Br (1.06 eV) > Mn₂O₃-Cl (0.696 eV) > Mn₂O₃-F (0.272 eV). It's known that doping with heteroatoms in crystals can prompt lattice distortion, damage its perfect and stable construction and create defects there. Therefore, all the halogen-Mn₂O₃ catalysts show lower O_v formation energy than the pristine Mn₂O₃. The lowest O_v formation energy in Mn₂O₃-F indicates that O atoms are the most vulnerable to escaping from the stretched Mn-O bonds. As for

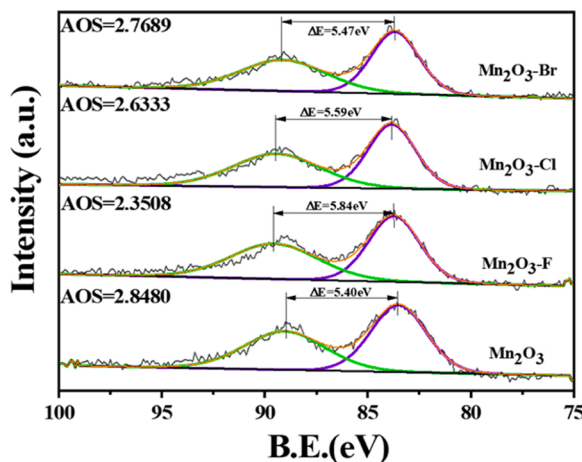


Fig. 8. High resolution XPS spectra of Mn 3s in Mn_2O_3 and halogen doped Mn_2O_3 .

$\text{Mn}_2\text{O}_3\text{-Cl}$ and $\text{Mn}_2\text{O}_3\text{-Br}$, although the O_v formation energy is decreased, the big-size Cl^- and Br^- can block those O_{vs} , presented as deteriorated catalytic activity despite the deformed crystal lattice and decreased O_v formation energy.

The charge density difference (CDD) and electron localization function (ELF) maps around the halogen (X: F, Cl, Br) atoms are analyzed to further investigate the localization behavior of electrons when oxygen vacancies are formed as the images show, when F atoms substitute O sites, many electrons localize around the F atoms and fewer

electrons are concentrated on coordinated O atoms. On the contrary, O sites substituted by Cl and Br atoms concentrate fewer electrons than those adjacent O atoms, which indicates the adjacent Mn-O bonds concatenate too hard to be broken up. Comparing the ELF maps, the electron localization area around the F atom enlarges as an adjacent oxygen vacancy appears, displayed as the circled area in Fig. 9. Oxygen vacancies can serve as the major exchange and transfer centers for electrons, in which the yellow and blue isosurfaces mean charge accumulation and depletion in the space.

3.5. Probable mechanism involved in photothermal degradation of toluene

Generally, reactive oxygen species like $\bullet\text{O}_2^-$ and $\bullet\text{OH}$ are responsible for the decomposition of toluene in both photocatalysis and photothermal catalysis [58]. The EPR signals of $\bullet\text{O}_2^-$ and $\bullet\text{OH}$ recorded on different Mn_2O_3 are displayed in Fig. 10a and b, which are silent in darkness, and sensitive under irradiation. Comparatively, these specific peaks on $\text{Mn}_2\text{O}_3\text{-F}$ are much intenser than other catalysts, relational contents of $\bullet\text{O}_2^-$ and $\bullet\text{OH}$ on $\text{Mn}_2\text{O}_3\text{-F}$ reaches 2.29×10^{-5} and 3.77×10^{-6} mol/L, respectively (Table S6), the amount of $\bullet\text{O}_2^-$ is almost 10 times that $\bullet\text{OH}$, which validates that the abundant O_{vs} in $\text{Mn}_2\text{O}_3\text{-F}$ contribute to adsorb many more O_2 from the air, delivering stronger signals with prevailing other Mn_2O_3 catalysts.

The superior catalytic activity on $\text{Mn}_2\text{O}_3\text{-F}$ can be illustrated by the adsorption behaviors of O_2 , H_2O , and toluene molecules through DFT calculations. The adsorption energies of O_2 and H_2O molecules on $\text{Mn}_2\text{O}_3\text{-F}$ are the lowest, -2.655 eV and -2.069 eV, respectively, which indicates O_2 and H_2O can be tightly adsorbed on $\text{Mn}_2\text{O}_3\text{-F}$ surface and activated there to form $\bullet\text{O}_2^-$ and $\bullet\text{OH}$. Since all the adsorption is

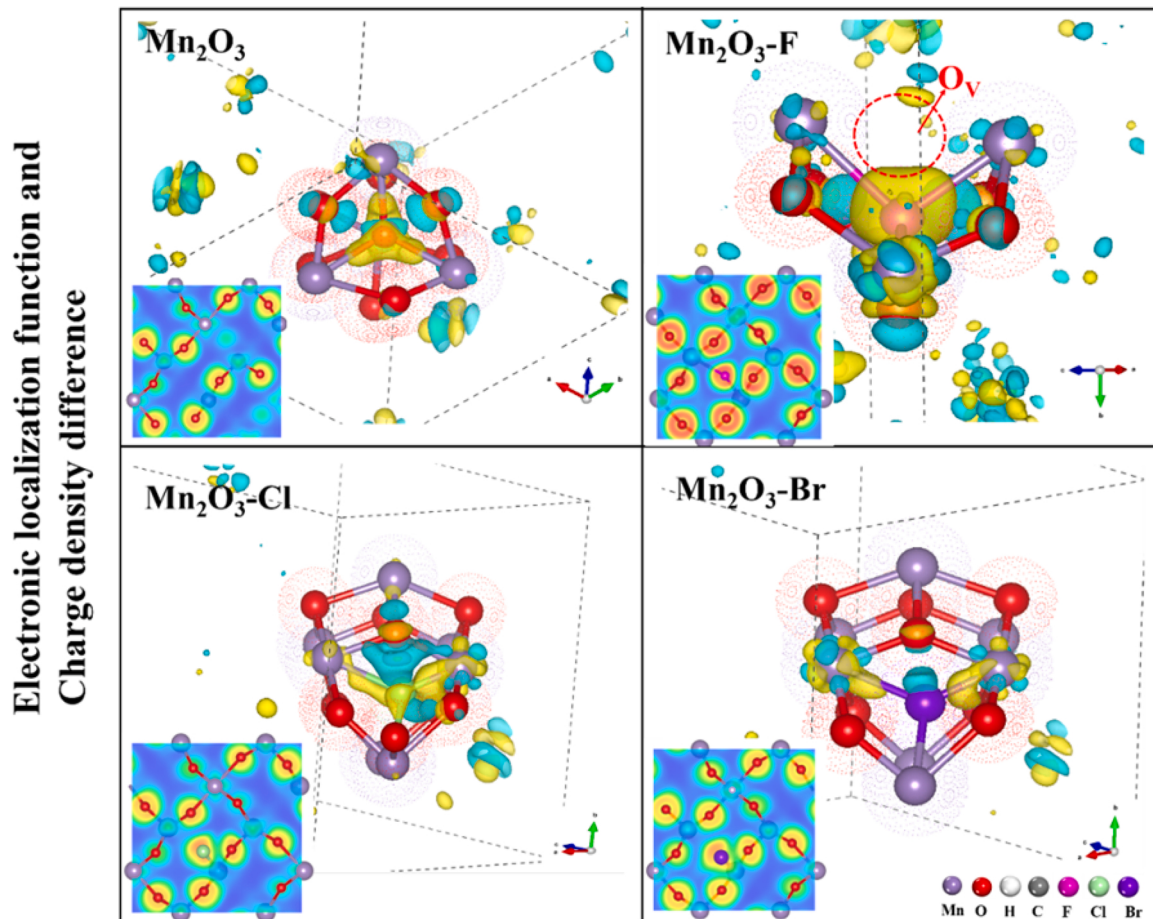


Fig. 9. Electronic localization function and charge density difference on Mn_2O_3 and halogen- Mn_2O_3 catalysts.

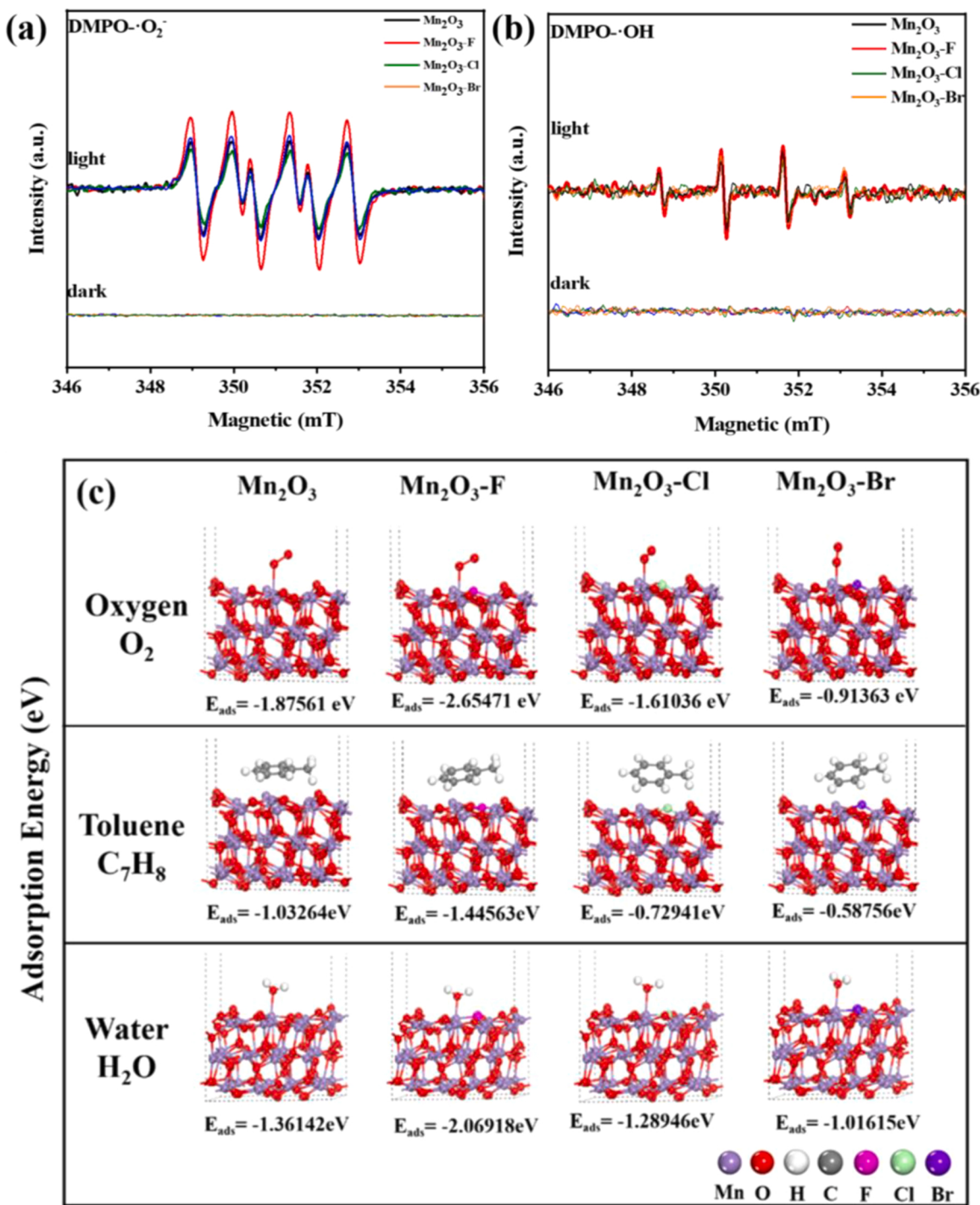


Fig. 10. DMPO spin-trapping EPR spectra of (a) DMPO-•O₂⁻ and (b) DMPO-•OH; (c) theoretical calculations (DFT) for adsorption energy of O₂, toluene, H₂O over different Mn₂O₃.

exothermic, a lower toluene adsorption energy means a higher affinity between toluene gases and catalyst, suggesting that toluene will be more easily oxidized by the reactive oxygen species on the catalyst interface [59]. As Fig. 10c shows, the E_{ads} (-1.446 eV) of toluene on Mn₂O₃-F is the lowest one, for the oxygen vacancies endows specific area with thick electron clouds that facilitate the adsorption of toluene. The above discoveries manifest that O₂, H₂O, and toluene molecules on the Mn₂O₃-F interface are easier to be anchored. As a result, the reaction probability between reactive oxygen species and toluene is greatly promoted.

To clarify the process of toluene degradation over Mn₂O₃-F, toluene

molecules and the intermediates on the catalyst surface were identified. Fig. S7 shows that the specific peak assigned to toluene is extremely high at the beginning, which disappears when the catalysis is finished at 40 min. There are some products from toluene degradation, containing benzaldehyde ($m/z = 106$), benzyl alcohol ($m/z = 108$), benzoic acid ($m/z = 122$), 1,3,5-trihydroxy benzene ($m/z = 126$), p-Hydroxybenzoic acid ($m/z = 138$), 2, 4-dihydroxycaproic acid ($m/z = 148$).

MS spectra of intermediates collected during the catalysis process at different times are shown in Fig. S8. 10 min after the beginning, many organic products appear, among which the highest signal values are indexed to benzaldehyde ($m/z = 106$) and benzyl alcohol ($m/z = 108$),

and the signal value of toluene ($m/z = 92$) is remarkably decreased.

20 min later, hydroquinone ($m/z = 110$), 1,3,5-trihydroxy benzene ($m/z = 126$), p-Hydroxybenzoic acid ($m/z = 138$), and 2,4-dihydroxy caproic acid ($m/z = 148$) are produced gradually while the amounts of benzaldehyde and benzyl alcohol ($m/z = 108$) minimize. When the reaction is completed, 1,3,5-trihydroxy benzene ($m/z = 126$), and 2, 4-dihydroxycaproic acid ($m/z = 148$) appear as main products.

Based on the aforementioned results, probable degradation pathways were proposed. As Fig. 11a shows, the methyl carbon as the electron-donating group is attacked by $\bullet\text{OH}$, and one of the hydrogen atoms in methyl falls off to form benzyl alcohol. Resultantly, the equilibrium state of the electrons inside the benzene ring is disturbed, and the stable carbon ring is activated with thickened electron density. Benzyl alcohol can be further oxidized to benzaldehyde by $\bullet\text{O}_2^-$ and O^- , and then to benzoic acid. The structural stability of the benzene ring is further damaged with the further loss of electrons along with the carbon group outside the benzene ring. As the carboxyl is an electron-denoting group, the benzene ring is further triggered with thickened electron clouds, and thus ready to accept the attacks from h^+ , $\bullet\text{O}_2^-$ and O^- . Afterward, the activated benzene ring and carboxyl are attacked by $\bullet\text{O}_2^-$

and O^- to form 1,3,5-trihydroxy benzene or hydroquinone, which transforms into CO_2 and H_2O ultimately.

The mechanism involved in the photothermal degradation of toluene is schematically depicted in Fig. 11b. As shown, under irradiation, the temperature of $\text{Mn}_2\text{O}_3\text{-F}$ can be approached to 213 °C, providing energy for the thermal motion in those reactions happening on $\text{Mn}_2\text{O}_3\text{-F}$. Oxygen vacancies induced by halogen doping are demonstrated in the peach rectangle. F atoms that replace O atoms attract the shared electrons from Mn to itself. Therefore, the deviated charge center stretches the adjacent Mn-O bonds and boosts the generation of abundant oxygen vacancies, helping to activate the adsorbed O_2 to $\bullet\text{O}_2^-$. Besides that, the redox couples of $\text{Mn}^{2+}/\text{Mn}^{3+}$, $\text{Mn}^{3+}/\text{Mn}^{4+}$ contribute to producing $\bullet\text{O}_2^-$ and $\bullet\text{OH}$ (green rectangle) for decomposing target toluene molecules. The above findings indicate that employing photothermal catalysts is a sustainable and efficient strategy to remove VOCs from the air.

4. Conclusion

The impact of representative halogen elements (F, Cl, Br) on regulating the activity of Mn_2O_3 catalysts was investigated through

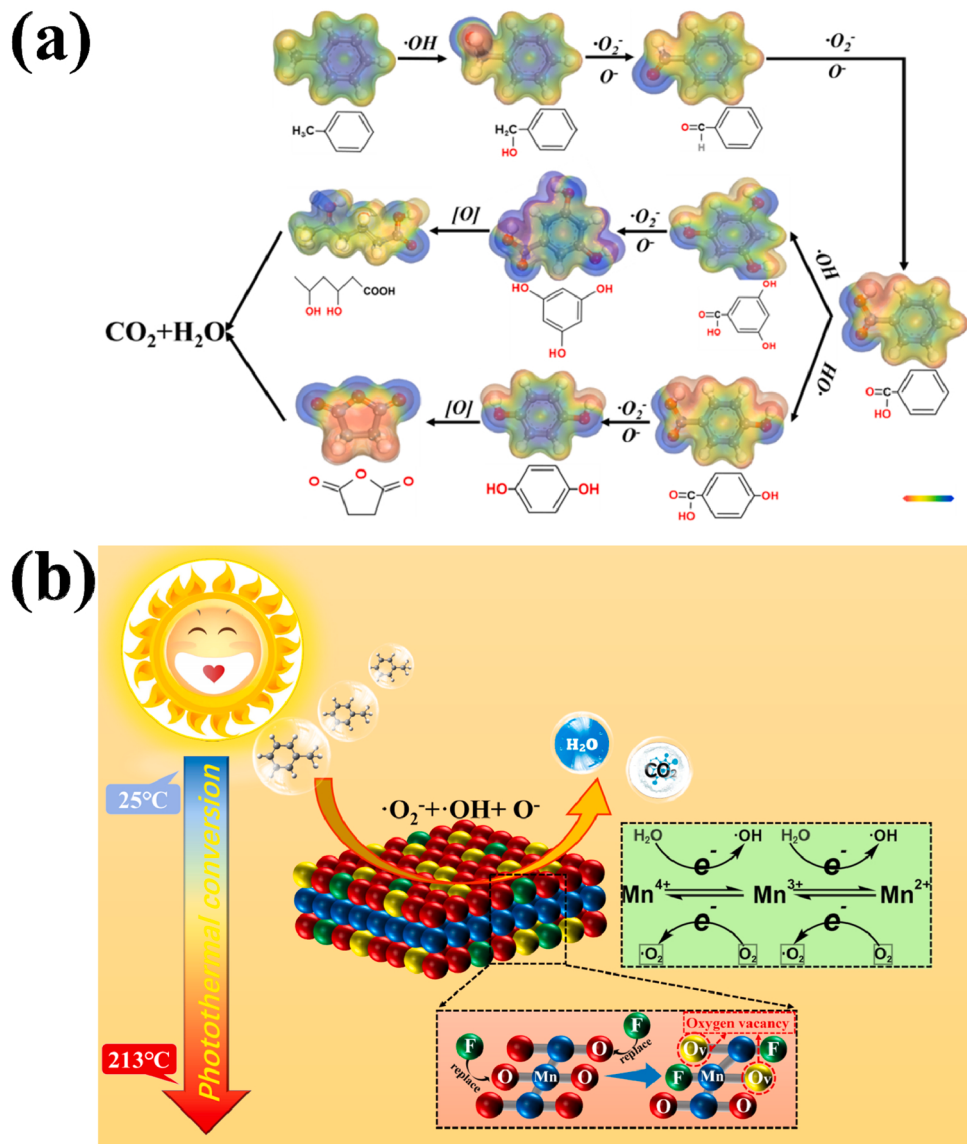


Fig. 11. (a) Proposed pathway of the photothermal catalytic degradation of toluene over $\text{Mn}_2\text{O}_3\text{-F}$. Electron density along carbon skeletons are visualized with red representing high electron-density area and blue representing the low electron-density area, (b) Schematic photocatalytic mechanism of toluene degradation with $\text{Mn}_2\text{O}_3\text{-F}$ catalyst.

photothermal degradation of toluene. Among F⁻, Cl⁻ and Br⁻, F⁻ has a similar diameter with O²⁻, and the highest electronegativity. It's easy and available for F⁻ to replace O²⁻ in Mn₂O₃ lattices. Owing to the marvelous ability to draw electrons, F⁻ dopant gives rise to the derivation of electron center between F-Mn bonds, which is far away from Mn ions, and therefore leads to the stretching of adjacent Mn-O bonds. As stretched Mn-O bonds weaken the binding force toward O atoms, which are prone to escape. Resultantly, the numbers of active Mn²⁺ and Mn⁴⁺ are increased and the distorted crystal lattices provide abundant oxygen vacancies. As for Cl⁻ and Br⁻, the big size makes them difficult to supplant the O atoms in Mn₂O₃ lattice, and the active sites can be covered when they are adsorbed on the Mn₂O₃ surface, exhibiting a deactivated effect on Mn₂O₃ activity in the photothermal degradation of toluene. Some Cl⁻ and Br⁻ can be doped in Mn₂O₃, but their lower electronegativity and big dimension lead to the shortened Mn-O bonds, posing a contrary influence on engineering Mn₂O₃ in comparison with F⁻. This work figures out the detailed reason for the influence of halogens on Mn₂O₃ catalysts in-depth and will enrich the scientific foundation of photothermal catalysts for VOC removal.

CRediT authorship contribution statement

Xiao Yu: Methodology, Investigation, Writing – original draft. **Mengyi Shi:** Investigation. **Yixuan Fan:** Conceptualization. **Wei Liu:** Investigation. **Lixia Yang:** Supervision, Writing – review & editing. **Jie Zhang:** Theoretical calculation. **Weili Dai:** Project administration. **Shuqu Zhang:** Methodology. **Xubiao Luo:** Resources. **Lei Zhou:** Methodology. **Shenglian Luo:** Resources.

Declaration of Competing Interest

The authors declare that they have no known competing financial interests or personal relationships that could have appeared to influence the work reported in this paper.

Acknowledgment

This work was supported by the National Natural Science Foundation of China (52070092, 52072165, 52100123). We are grateful for the financial support received for this project.

Appendix A. Supporting information

Supplementary data associated with this article can be found in the online version at [doi:10.1016/j.apcatb.2022.121236](https://doi.org/10.1016/j.apcatb.2022.121236).

References

- [1] X. Wang, Y. Liu, T. Zhang, Y. Luo, Z. Lan, K. Zhang, J. Zuo, L. Jiang, R. Wang, Geometrical-site-dependent catalytic activity of ordered mesoporous Co-based spinel for benzene oxidation: in situ DRIFTS study coupled with Raman and XAFS spectroscopy, *ACS Catal.* 7 (3) (2017) 1626–1636, <https://doi.org/10.1021/acscatal.6b03547>.
- [2] L. Yang, J. Guo, T. Yang, C. Guo, S. Zhang, S. Luo, W. Dai, B. Li, X. Luo, Y. Li, Self-assembly Cu₂O nanowire arrays on Cu mesh: a solid-state, highly-efficient, and stable photocatalyst for toluene degradation under sunlight, *J. Hazard. Mater.* 402 (2021) 123–141, <https://doi.org/10.1016/j.jhazmat.2020.123741>.
- [3] K. Su, H. Liu, B. Zeng, Z. Zhang, N. Luo, Z. Huang, Z. Gao, F. Wang, Visible-light-driven selective oxidation of toluene into benzaldehyde over nitrogen-modified Nb₂O₅ nanomeshes, *ACS Catal.* 10 (2) (2019) 1324–1333, <https://doi.org/10.1021/acscatal.9b04215>.
- [4] N.G. Asenjo, P. Alvarez, M. Granda, C. Blanco, R. Santamaría, R. Menendez, High performance activated carbon for benzene/toluene adsorption from industrial wastewater, *J. Hazard. Mater.* 192 (3) (2011) 1525–1532, <https://doi.org/10.1016/j.jhazmat.2011.06.072>.
- [5] U. Anggarini, L. Yu, H. Nagasawa, M. Kanezashi, T. Tsuru, Microporous nickel-coordinated aminosilica membranes for improved pervaporation performance of methanol/toluene separation, *ACS Appl. Mater. Interfaces* 13 (19) (2021) 23247–23259, <https://doi.org/10.1021/acsami.1c05012>.
- [6] H. Li, W. Ho, J. Cao, D. Park, S.C. Lee, Y. Huang, Active complexes on engineered crystal facets of MnO_x-CeO₂ and scale-up demonstration on an air cleaner for indoor formaldehyde removal, *Environ. Sci. Technol.* 53 (18) (2019) 10906–10916, <https://doi.org/10.1021/acs.est.9b03197>.
- [7] Y. Zheng, Q. Liu, C. Shan, Y. Su, K. Fu, S. Lu, R. Han, C. Song, N. Ji, D. Ma, Defective ultrafine MnO_x nanoparticles confined within a carbon matrix for low-temperature oxidation of volatile organic compounds, *Environ. Sci. Technol.* 55 (8) (2021) 5403–5411, <https://doi.org/10.1021/acs.est.0c08335>.
- [8] Z. Bo, S. Yang, J. Kong, J. Zhu, Y. Wang, H. Yang, X. Li, J. Yan, K. Cen, X. Tu, Solar-enhanced plasma-catalytic oxidation of toluene over a bifunctional graphene fin foam decorated with nanofin-like MnO₂, *ACS Catal.* 10 (7) (2020) 4420–4432, <https://doi.org/10.1021/acscatal.9b04844>.
- [9] Z. Wu, D. Zhu, Z. Chen, S. Yao, J. Li, E. Gao, W. Wang, Enhanced energy efficiency and reduced nanoparticle emission on plasma catalytic oxidation of toluene using Au/ γ -Al₂O₃ nanocatalyst, *Chem. Eng. J.* 427 (2022), <https://doi.org/10.1016/j.cej.2021.130983>.
- [10] J. Zhao, Z. Zhao, N. Li, J. Nan, R. Yu, J. Du, Visible-light-driven photocatalytic degradation of ciprofloxacin by a ternary Mn₂O₃/Mn₃O₄/MnO₂ valence state heterojunction, *Chem. Eng. J.* 353 (2018) 805–813, <https://doi.org/10.1016/j.cej.2018.07.163>.
- [11] H. Wang, Z. Huang, Z. Jiang, Z. Jiang, Y. Zhang, Z. Zhang, W. Shangguan, Trifunctional C@MnO catalyst for enhanced stable simultaneously catalytic removal of formaldehyde and ozone, *ACS Catal.* 8 (4) (2018) 3164–3180, <https://doi.org/10.1021/acscatal.8b00309>.
- [12] C. Jiang, H. Wang, S. Lin, F. Ma, Y. Wang, H. Ji, Low-temperature photothermal catalytic oxidation of toluene on a core/shell SiO₂@Pt@ZrO₂ nanostructure, *Ind. Eng. Chem. Res.* 58 (36) (2019) 16450–16458, <https://doi.org/10.1021/acs.iecr.9b02850>.
- [13] J. Li, M. Zhang, E.A. Elimian, X. Lv, J. Chen, H. Jia, Convergent ambient sunlight-powered multifunctional catalysis for toluene abatement over in situ exsolution of Mn₃O₄ on perovskite parent, *Chem. Eng. J.* 412 (2021), <https://doi.org/10.1016/j.cej.2021.128560>.
- [14] M. Słomińska, S. Król, J. Namieśnik, Removal of BTEX compounds from waste gases; destruction and recovery techniques, critical reviews, *Environ. Sci. Technol.* 43 (14) (2013) 1417–1445, <https://doi.org/10.1080/10643389.2011.647760>.
- [15] M. Wen, G. Li, H. Liu, J. Chen, T. An, H. Yamashita, Metal-organic framework-based nanomaterials for adsorption and photocatalytic degradation of gaseous pollutants: recent progress and challenges, *Environ. Sci.: Nano* 6 (4) (2019) 1006–1025, <https://doi.org/10.1039/c8en01167b>.
- [16] M. Woellner, S. Hausdorf, N. Klein, P. Mueller, M.W. Smith, S. Kaskel, Adsorption and detection of hazardous trace gases by metal-organic frameworks, *Adv. Mater.* 30 (37) (2018), e1704679, <https://doi.org/10.1002/adma.201704679>.
- [17] D. Mateo, J.L. Cerrillo, S. Durini, J. Gascon, Fundamentals and applications of photo-thermal catalysis, *Chem. Soc. Rev.* 50 (3) (2021) 2173–2210, <https://doi.org/10.1039/d0cs00357c>.
- [18] S. Lu, F. Liu, P. Qiu, M. Qiao, Y. Li, Z. Cheng, N. Xue, X. Hou, C. Xu, Y. Xiang, F. Peng, Z. Guo, Photothermal-assisted photocatalytic degradation with ultrahigh solar utilization: towards practical application, *Chem. Eng. J.* 379 (2020), <https://doi.org/10.1016/j.cej.2019.122382>.
- [19] H. Liu, Y. Li, Y. Yang, M. Mao, M. Zeng, L. Lan, L. Yun, X. Zhao, Highly efficient UV-Vis-infrared catalytic purification of benzene on CeMn₃O₄/TiO₂ nanocomposite, caused by its high thermocatalytic activity and strong absorption in the full solar spectrum region, *J. Mater. Chem. A* 4 (25) (2016), <https://doi.org/10.1039/C6TA03181A>.
- [20] Z. Shi, L. Lan, Y. Li, Y. Yang, Q. Zhang, J. Wu, G. Zhang, X. Zhao, Co₃O₄/TiO₂ nanocomposite formation leads to improvement in ultraviolet-visible-infrared-driven thermocatalytic activity due to photoactivation and photocatalysis-thermocatalysis synergistic effect, *ACS Sustain. Chem. Eng.* 6 (12) (2018) 16503–16514, <https://doi.org/10.1021/acssuschemeng.8b03602>.
- [21] J.-J. Li, E.-Q. Yu, S.-C. Cai, X. Chen, J. Chen, H.-P. Jia, Y.-X. Xu, Noble metal free, CeO₂/LaMnO₃ hybrid achieving efficient photo-thermal catalytic decomposition of volatile organic compounds under IR light, *Appl. Catal. B: Environ.* 240 (2019) 141–152, <https://doi.org/10.1016/j.apcatb.2018.08.069>.
- [22] P. Wu, X. Jin, Y. Qiu, D. Ye, Recent progress of thermocatalytic and photo-thermocatalytic oxidation for VOCs purification over manganese-based oxide catalysts, *Environ. Sci. Technol.* 55 (8) (2021) 4268–4286, <https://doi.org/10.1021/acs.est.0c08179>.
- [23] C. Chai, C. Fan, J. Liu, X. Zhang, Y. Wang, R. Li, D. Duan, Y. Wang, Photoinduced g-C₃N₄-promoted Mn²⁺/Mn³⁺/Mn⁴⁺ redox cycles for activation of peroxyxonosulfate, *J. Solid State Chem.* 277 (2019) 466–474, <https://doi.org/10.1016/j.jssc.2019.07.005>.
- [24] M. Mao, Y. Li, J. Hou, M. Zeng, X. Zhao, Extremely efficient full solar spectrum light driven thermocatalytic activity for the oxidation of VOCs on OMS-2 nanorod catalyst, *Appl. Catal. B: Environ.* 174–175 (2015) 496–503, <https://doi.org/10.1016/j.apcatb.2015.03.044>.
- [25] Y. Tang, Y. Tao, T. Zhou, B. Yang, Q. Wang, Z. Zhu, A. Xie, S. Luo, C. Yao, X. Li, Direct Z-scheme La_{1-x}Ce_xMnO₃ catalyst for photothermal degradation of toluene, *Environ. Sci. Pollut. Res. Int.* 26 (36) (2019) 36832–36844, <https://doi.org/10.1007/s11356-019-06856-7>.
- [26] Y. Shi, R. Li, Y. Jin, S. Zhuo, L. Shi, J. Chang, S. Hong, K.-C. Ng, P. Wang, A 3D photothermal structure toward improved energy efficiency in solar steam generation, *Joule* 2 (6) (2018) 1171–1186, <https://doi.org/10.1016/j.joule.2018.03.013>.
- [27] Y. Wang, Y. Zhao, J. Liu, Z. Li, G.I.N. Waterhouse, R. Shi, X. Wen, T. Zhang, Manganese oxide modified nickel catalysts for photothermal CO hydrogenation to light olefins, *Adv. Energy Mater.* 10 (5) (2019), <https://doi.org/10.1002/aenm.201902860>.

[28] A. Xie, H. Wang, S. Qi, X. Li, Z. Zhu, W. Zhang, Q. Wang, Y. Tang, S. Luo, Mesoporous $\text{SmMnO}_3/\text{CuMnO}$ catalyst for photothermal synergistic degradation of gaseous toluene, *Ceram. Int.* (2021), <https://doi.org/10.1016/j.ceramint.2021.08.026>.

[29] W. Yang, Y. Wang, W. Yang, H. Liu, Z. Li, Y. Peng, J. Li, Surface in situ doping modification over Mn_2O_3 for toluene and propene catalytic oxidation: the effect of isolated $\text{Cu}^{\delta+}$ insertion into the mezzanine of surface MnO_2 cladding, *ACS Appl. Mater. Interfaces* 13 (2) (2021) 2753–2764, <https://doi.org/10.1021/acsami.0c19972>.

[30] W. Yang, Y. Peng, Y. Wang, Y. Wang, H. Liu, Za Su, W. Yang, J. Chen, W. Si, J. Li, Controllable redox-induced in-situ growth of MnO_2 over Mn_2O_3 for toluene oxidation: Active heterostructure interfaces, *Appl. Catal. B: Environ.* 278 (2020), <https://doi.org/10.1016/j.apcatb.2020.119279>.

[31] Y. Zheng, Y. Su, C. Pang, L. Yang, C. Song, N. Ji, D. Ma, X. Lu, R. Han, Q. Liu, Interface-enhanced oxygen vacancies of CoCuO_x catalysts in situ grown on monolithic cu foam for VOC catalytic oxidation, *Environ. Sci. Technol.* (2021), <https://doi.org/10.1021/acs.est.1c05855>.

[32] R. Yang, X. Lu, X. Huang, Z. Chen, X. Zhang, M. Xu, Q. Song, L. Zhu, Bi-component $\text{Cu}_2\text{O}-\text{CuCl}$ composites with tunable oxygen vacancies and enhanced photocatalytic properties, *Appl. Catal. B: Environ.* 170–171 (2015) 225–232, <https://doi.org/10.1016/j.apcatb.2015.01.046>.

[33] X. Ren, M. Gao, Y. Zhang, Z. Zhang, X. Cao, B. Wang, X. Wang, Photocatalytic reduction of CO_2 on BiOX : Effect of halogen element type and surface oxygen vacancy mediated mechanism, *Appl. Catal. B: Environ.* 274 (2020), <https://doi.org/10.1016/j.apcatb.2020.119063>.

[34] A. Hattori, H. Tada, High photocatalytic activity of F-doped TiO_2 film on glass, *J. Sol-Gel Sci. Technol.* 22 (2001) 47–52, <https://doi.org/10.1023/A:1011260219229>.

[35] M.S. Vohra, S. Kim, W. Choi, Effects of surface fluorination of TiO_2 on the photocatalytic degradation of tetramethylammonium, *J. Photoch. Photobio. A: Chem.* 160 (2003) 55–60, [https://doi.org/10.1016/S1010-6030\(03\)00221-1](https://doi.org/10.1016/S1010-6030(03)00221-1).

[36] H. Sun, S. Wang, H.M. Ang, M.O. Tadé, Q. Li, Halogen element modified titanium dioxide for visible light photocatalysis, *Chem. Eng. J.* 162 (2010) 437–447, <https://doi.org/10.1016/j.cej.2010.05.069>.

[37] G. Kresse, J. Furthmüller, Efficient iterative schemes for Ab initio total-energy calculations using a plane-wave basis set, *Phys. Rev. B* 54 (1996) 11169–11186, <https://doi.org/10.1103/PhysRevB.54.11169>.

[38] J.P. Perdew, K. Burke, M. Ernzerhof, Generalized gradient approximation made simple, *Phys. Rev. Lett.* 77 (1996) 3865–3868, <https://doi.org/10.1103/PhysRevLett.77.3865>.

[39] G. Kresse, D. Joubert, From ultrasoft pseudopotentials to the projector augmented-wave method, *Phys. Rev. B* 59 (1999) 1758–1775, <https://doi.org/10.1103/PhysRevB.59.1758>.

[40] P.E. Blochl, Projector augmented-wave method, *Phys. Rev. B Condens Matter* 50 (1994) 17953–17979, <https://doi.org/10.1103/PhysRevB.50.17953>.

[41] S. Grimme, J. Antony, S. Ehrlich, H. Krieg, A consistent and accurate ab initio parametrization of density functional dispersion correction (DFT-D) for the 94 elements H–Pu, *J. Chem. Phys.* 132 (15) (2010), 154104, <https://doi.org/10.1063/1.3382344>.

[42] G. Henkelman, B.P. Uberuaga, H. Jónsson, A climbing image nudged elastic band method for finding saddle points and minimum energy paths, *J. Chem. Phys.* 113 (22) (2000) 9901–9904, <https://doi.org/10.1063/1.1329672>.

[43] L. Cheng, Y. Men, J. Wang, H. Wang, W. An, Y. Wang, Z. Duan, J. Liu, Crystal facet-dependent reactivity of $\alpha\text{-Mn}_2\text{O}_3$ microcrystalline catalyst for soot combustion, *Appl. Catal. B: Environ.* 204 (2017) 374–384, <https://doi.org/10.1016/j.apcatb.2016.11.041>.

[44] V.D. Mote, B.N. Dole, Structural, optical, and magnetic properties of Mn-doped ZnS nanoparticles, *J. Mater. Sci. Mater. Electron.* 32 (2020) 420–429, <https://doi.org/10.1007/s10854-020-04790-w>.

[45] M.V. Konishcheva, D.I. Potemkin, P.V. Snytnikov, V.P. Pakharukova, V. A. Sobyanin, Preferential methanation of CO using halogen-doped (F, Cl, Br) ceria-supported nickel catalysts, *Energy Technol.* 5 (2017) 1522–1525, <https://doi.org/10.1002/ente.201700088>.

[46] H. Kunioku, A. Nakada, M. Higashi, O. Tomita, H. Kageyama, R. Abe, Improved water oxidation under visible light on oxyhalide $\text{Bi}_4\text{MO}_8\text{X}$ ($\text{M} = \text{Nb}, \text{Ta}; \text{X} = \text{Cl}, \text{Br}$) photocatalysts prepared using excess halogen precursors, *Sustain. Energy Fuels* 2 (2018) 1474–1480, <https://doi.org/10.1039/c8se00097b>.

[47] S. Zhang, Z. Zhang, Y. Si, B. Li, F. Deng, L. Yang, X. Liu, W. Dai, S. Luo, Gradient hydrogen migration modulated with self-adapting S vacancy in copper-doped ZnIn_2S_4 nanosheet for photocatalytic hydrogen evolution, *ACS Nano* (2021), <https://doi.org/10.1021/acsnano.1c05834>.

[48] H. Yan, Q. Shen, Y. Sun, S. Zhao, R. Lu, M. Gong, Y. Liu, X. Zhou, X. Jin, X. Feng, X. Chen, D. Chen, C. Yang, Tailoring facets of $\alpha\text{-Mn}_2\text{O}_3$ microcrystalline catalysts for enhanced selective oxidation of glycerol to glycolic acid, *ACS Catal.* 11 (11) (2021) 6371–6383, <https://doi.org/10.1021/acscatal.1c01566>.

[49] D. Jampaiah, V.K. Velisjoju, P. Venkataswamy, V.E. Coyle, A. Nafady, B.M. Reddy, S.K. Bhargava, Nanowire morphology of mono- and bidoped alpha- MnO_2 catalysts for remarkable enhancement in soot oxidation, *ACS Appl. Mater. Interfaces* 9 (38) (2017) 32652–32666, <https://doi.org/10.1021/acsmi.7b07656>.

[50] M. Šťastný, G. Issa, D. Popelková, J. Ederer, M. Kormunda, S. Kríženecká, J. Henych, Nanostructured manganese oxides as highly active catalysts for enhanced hydrolysis of bis(4-nitrophenyl) phosphate and catalytic decomposition of methanol, *Catal. Sci. Technol.* 11 (5) (2021) 1766–1779, <https://doi.org/10.1039/d0cy02112a>.

[51] F. Duo, Y. Wang, X. Mao, X. Zhang, Y. Wang, C. Fan, A $\text{BiPO}_4/\text{BiOCl}$ heterojunction photocatalyst with enhanced electron-hole separation and excellent photocatalytic performance, *Appl. Surf. Sci.* 340 (2015) 35–42, <https://doi.org/10.1016/j.apsusc.2015.02.175>.

[52] M.K. Datta, K. Kadakia, O.I. Velikokhatnyi, P.H. Jampani, S.J. Chung, J.A. Poston, A. Manivannan, P.N. Kumta, High performance robust F-doped tin oxide based oxygen evolution electro-catalysts for PEM based water electrolysis, *J. Mater. Chem. A* 1 (12) (2013), <https://doi.org/10.1039/c3ta01458d>.

[53] J. Chen, X. Chen, X. Chen, W. Xu, Z. Xu, H. Jia, J. Chen, Homogeneous introduction of CeO_2 into MnO_x -based catalyst for oxidation of aromatic VOCs, *Appl. Catal. B: Environ.* 224 (2018) 825–835, <https://doi.org/10.1016/j.apcatb.2017.11.036>.

[54] X. Zhu, B. Cheng, J. Yu, W. Ho, Halogen poisoning effect of Pt-TiO_2 for formaldehyde catalytic oxidation performance at room temperature, *Appl. Surf. Sci.* 364 (2016) 808–814, <https://doi.org/10.1016/j.apsusc.2015.12.115>.

[55] Y. Wang, X. Zhu, M. Crocker, B. Chen, C. Shi, A comparative study of the catalytic oxidation of HCHO and CO over $\text{Mn}_{0.75}\text{Co}_{2.25}\text{O}_4$ catalyst: the effect of moisture, *Appl. Catal. B: Environ.* 160–161 (2014) 542–551, <https://doi.org/10.1016/j.apcatb.2014.06.011>.

[56] X. Feng, J. Yang, X. Duan, Y. Cao, B. Chen, W. Chen, D. Lin, G. Qian, D. Chen, C. Yang, X. Zhou, Enhanced catalytic performance for propene epoxidation with H_2 and O_2 over bimetallic $\text{Au-Ag}/\text{uncalcined titanium silicate-1}$ catalysts, *ACS Catal.* 8 (9) (2018) 7799–7808, <https://doi.org/10.1021/acscatal.8b01324>.

[57] M.C. Bernard, A. Hugot-LeGoff, B.V. Thi, S.C. De Torresi, Electrochromic reactions in manganese oxides: Raman analysis, *J. Electrochem. Soc.* 140 (1993) 3065–3070, <https://doi.org/10.1149/1.2220986>.

[58] L. Yang, J. Guo, J. Zhang, S. Zhang, W. Dai, X. Xiao, X. Luo, S. Luo, Utter degradation of toluene with inhibiting the generation of benzene by self-supporting Bi_2MoO_6 nanoflakes featuring OV-enriched interface, *Chem. Eng. J.* 427 (2022), <https://doi.org/10.1016/j.cej.2021.131550>.

[59] P. Chen, W. Cui, H. Wang, X.A. Dong, J.Y. Li, Y.J. Sun, Y. Zhou, Y.X. Zhang, F. Dong, The importance of intermediates ring-opening in preventing photocatalyst deactivation during toluene decomposition, *Appl. Catal. B: Environ.* 272 (2020), <https://doi.org/10.1016/j.apcatb.2020.118977>.